Contrib Mineral Petrol (2017) 172:94
https://doi.org/10.1007/s00410-017-1410-9

ORIGINAL PAPER

Unravelling the magmatic system beneath a monogenetic volcanic complex (Jagged Rocks Complex, Hopi Buttes, AZ, USA)

G. Re[1] · J. M. Palin[1] · J. D. L. White[1] · M. Parolari[2]

Received: 7 January 2017 / Accepted: 8 October 2017 / Published online: 6 November 2017

Abstract The Jagged Rocks complex is the eroded remnant of the plumbing systems of closely spaced monogenetic alkaline volcanic centres in the southern Hopi Buttes Volcanic Field (AZ, USA). It contains different clinopyroxene populations with distinctive textures and geochemical patterns. In the Northwestern part of the complex, which exposes the best developed system of conduits, most of the clinopyroxenes consist of large- to medium-sized resorbed cores overgrown by euhedral rims (type 1), small moderately resorbed greenish cores with the same overgrown rims (type 2), and phlogopite as an accessory phase. By contrast, in the Southern part of the complex the majority of clinopyroxenes are euhedral with oscillatory zonation (type 3) and are accompanied by minor euhedral olivine. The differences between these mineral assemblages indicate a composite history of crystallization and magmatic evolution for the two parts of the complex, governed by different mechanisms and ascent patterns from a single source at ~ 50 km depth (16 kbar). The Northwest system preserves a high-pressure assemblage that cooled rapidly from near-liquidus conditions, suggesting direct ascent from the source to the surface at high-to-moderate transport rates (average ~ 1.25 m/s). By contrast, the Southern system represents magma that advanced upward at much lower overall ascent rates, stalling at times to form small-volume mid-crustal storage zones (e.g., sills or a network of sheeted intrusions); this allowed the re-equilibration of the magma at lower pressure (~ 30 km; 8 kbar), and led to nucleation and growth of euhedral clinopyroxene and olivine phenocrysts.

Keywords Monogenetic volcanism · Clinopyroxene · Ascent rate

Introduction

Monogenetic volcanic fields are clusters of small-volume (> 1 km^3) volcanic centres that result from spatially and temporally dispersed volcanism; they contrast with long-lived polygenetic central volcanoes (Connor and Conway 2000; Kereszturi and Németh 2012). Each volcano within a field, which can include maars, tuff rings, cinder cones, scoria cones, and small shields, is considered the result of a single eruptive cycle spanning from several days to years (Connor and Conway 2000; Valentine and Gregg 2008; Németh 2010). Despite their small size and limited lifetime, individual monogenetic volcanoes can have a complex architecture that reflects multiple eruption phases, with shifts between different levels of explosive activity and effusive intervals (Doubik and Hill 1999; Houghton et al. 1999; Ort and Carrasco-Nunez 2009; McGee et al. 2012; Valentine and Cortés 2013). Some studies have shown that single eruptive centres were fed by different magma batches over the short period involved in building a monogenetic volcano (Luhr 2001; Nemeth et al. 2003, 2014; Strong and Wolff 2003; Blondes et al. 2008; Smith et al. 2008; Brenna et al. 2010, 2011; Erlund et al. 2009; McGee et al. 2012; Sohn et al. 2012; Boyce et al. 2015; Jankovics et al. 2015; Moorhouse et al. 2015).

Communicated by Mark S. Ghiorso.

Electronic supplementary material The online version of this article (doi:10.1007/s00410-017-1410-9) contains supplementary material, which is available to authorized users.

✉ G. Re
ilpeppere@gmail.com

[1] University of Otago, Dunedin, New Zealand

[2] UNAM, Querétaro, Mexico

In this paper, we present a study of the Jagged Rocks Complex, which exceptionally exposes the shallow plumbing system of a cluster of monogenetic volcanoes. Detailed textural and chemical investigation of minerals, integrated with X-ray fluorescence (XRF) groundmass geochemistry, yields insight into the processes affecting magma during ascent to form a complex of two or more closely spaced monogenetic volcanoes. Compositional changes in the crystal-growth stratigraphy (zonation) record modification of the magmatic environment, and provide evidence of geochemical complexities in the plumbing of these monogenetic volcanoes and of discrete magma batches that went through different levels (degrees) of evolution. There is evidence for differentiation of magma by fractional crystallization, and also for kinetic effects on crystal-growth in response to different rates of cooling and decompression (Ginibre et al. 2007; Streck 2008; Mollo et al. 2010, 2015; Scarlato et al. 2014; Jankovics et al. 2015). Patterns of magma ascent, staging, and evolution ultimately help to control eruptive style, with potential implications for changes in volcanic hazard over relatively short time intervals (Brenna et al. 2010).

Geological setting and volcanological features

The Hopi Buttes Volcanic Field (7 Ma; Dallegge et al. 2003) was emplaced on the Colorado Plateau within a flat-playa (lacustrine) environment during an episode of Late Miocene alkaline volcanism (White 1991). The Hopi Buttes erupted through a relatively thick continental lithosphere (LAB ~ 90 km, Moho ~ 50 km; Levander et al. 2011; Reid et al. 2012), which consists of a paleoproterozoic igneous and metamorphic basement overlain by flat-lying Paleozoic to Cenozoic sedimentary sequences. The southern portion of the Hopi Buttes (Fig. 1), where the Jagged Rocks Complex is located, had up to 400 m of post-volcanic erosion that brought to light portions of the shallow plumbing system of closely spaced monogenetic centres, including dikes, sills, and pyroclastic massifs (remnants of volcanic conduits; Re et al. 2016). Conversely, in the northern Hopi Buttes, above the undisturbed sedimentary sequences, subaerial volcaniclastic products, and exhumed volcanic landforms crop out as lava flows, tephra fall layers, and tuff ring deposits that interfinger with Miocene sedimentary deposits (White 1990). Current exposure level at the Jagged Rocks Complex is between 365 and 245 m below the pre-eruptive surface, based upon the well-known and uniform regional stratigraphy of the area (Billingsley et al. 2013).

The Jagged Rocks Complex (Fig. 2) extends over a 2 km^2 area and consists of different intrusive and subvolcanic deposits: (1) the Northwest *en echelon* dike system, which holds five pyroclastic massifs at its midpoint (Re et al. 2016), (2) the Southwest dike, whose eastward portion is truncated by a debris-filled diatreme, and (3) the Central and the Southeast dikes, which are surrounded by two inward-dipping transgressive sills associated with a saucer-shaped

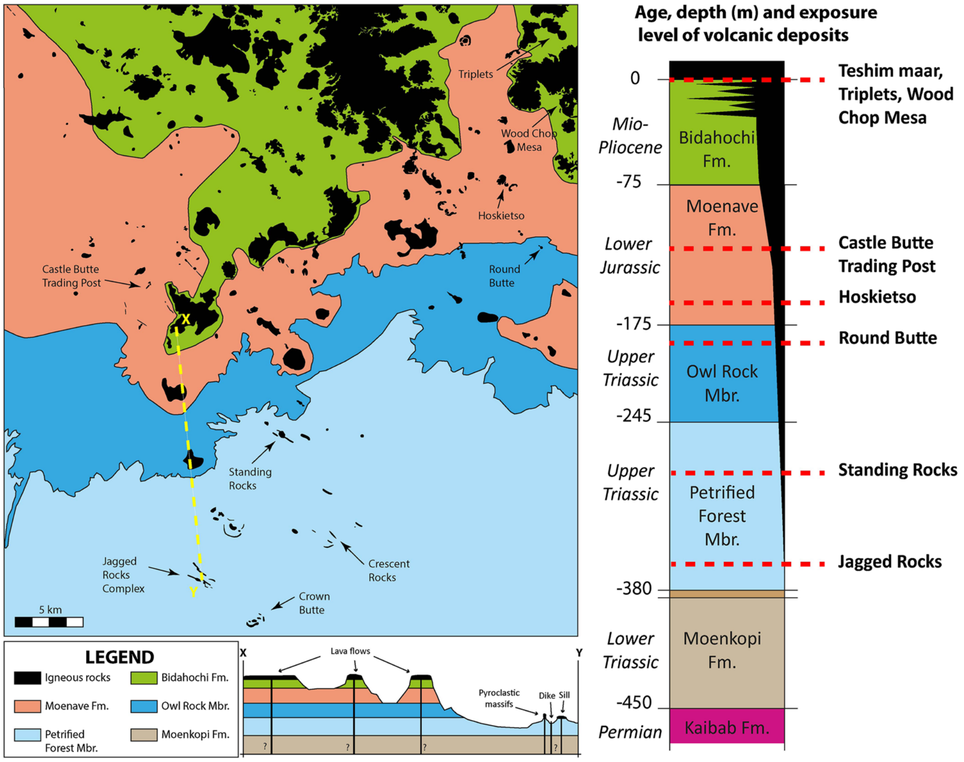

Fig. 1 Simplified geological map of the Hopi Buttes Volcanic Field, modified from Muirhead et al. (2016). The stratigraphic column illustrates the sedimentary country rock succession across the Hopi Buttes, and the epoch of deposition for each unit. Igneous rocks are in black. Depth is based on the average thicknesses from Billingsley et al. (2013) calculated from the pre-eruptive paleosurface. On the map, the locations of some volcanoes are noted and their deposits placed at corresponding depths in the stratigraphic column. Schematic cross-section (*X*–*Y*) oriented north–south reveals the southward deepening erosion surface

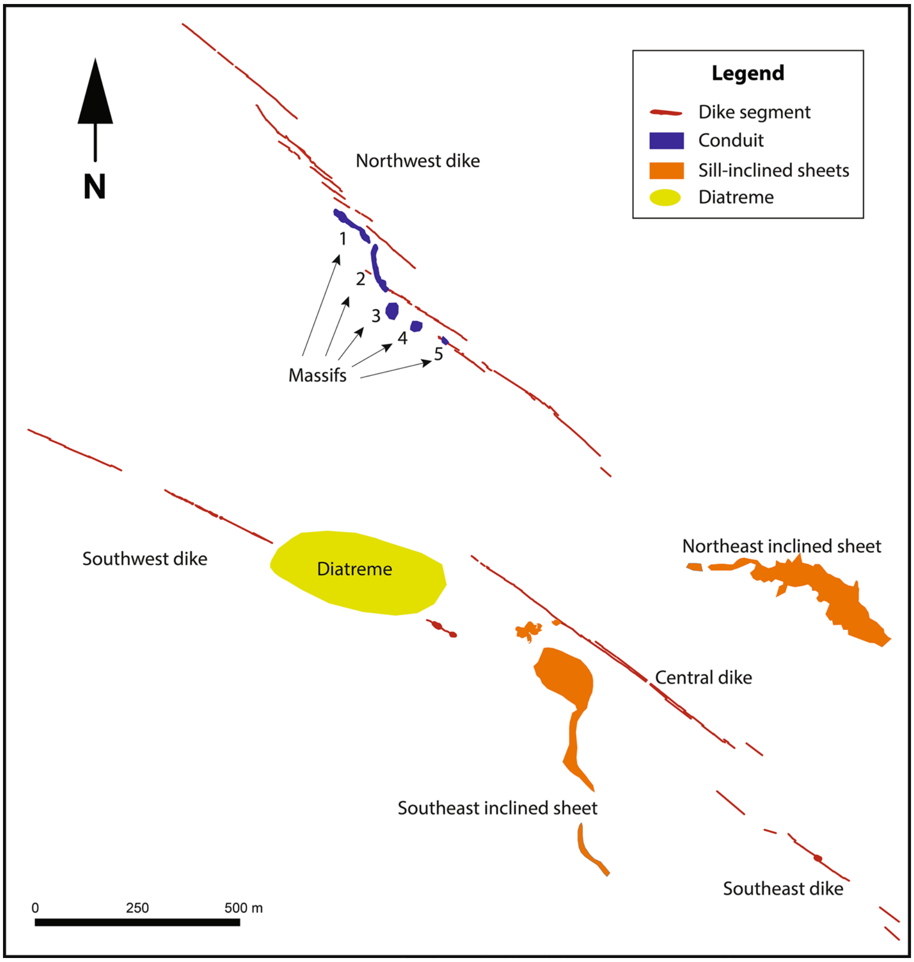

Fig. 2 Simplified map of Jagged Rocks Complex, modified from Re et al. (2015). Red lines represent the dike segments, orange pattern marks transgressive sills, purple denotes pyroclastic massifs, and the diatreme is in green. Are annotated on the map the massif numbers and the name of intrusive sheets. We refer to the northwest dikes and massifs together as the Northwest system, whereas the southwest, central, and southeast dike together with the southeast inclined and northeast inclined sheets are included in the Southern system

intrusion (Re et al. 2015; Muirhead et al. 2016). The Northwest system reveals not only distinctive structural and volcanological features (Re et al. 2015, 2016), but also a distinctive mineralogical assemblage visible at the outcrop scale, with abundant and ubiquitous clinopyroxene megacrysts (up to 5 cm) and rare phlogopite (Fig. 3); both appear nowhere else across the Jagged Rocks Complex. This inequigranular texture contrasts strongly with the equigranular texture of the Southern system, which comprises all the other dikes and the saucer-shaped intrusion. Rocks of the Southern system have a fine- to medium-grained microcrystalline groundmass and lack notable large crystals.

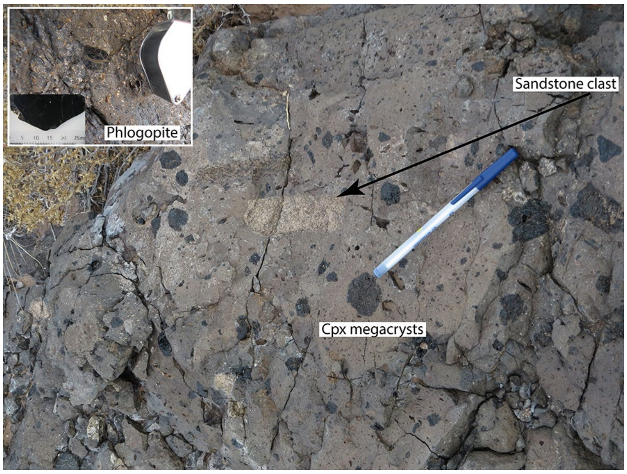

Fig. 3 Top view of a coherent dike along the NW system. An overall homogeneous groundmass bears very large clinopyroxene megacrysts (type 1). The inset picture shows a phlogopite megacryst

Sampling and analytical methods

Rock samples for this study were collected from intrusive and volcaniclastic deposits across the Jagged Rocks Complex. Samples were chosen, after hand specimens observations, from the freshest and least altered rocks, with the finest-grained and mostly equigranular groundmasses, smallest and least abundant phenocrysts, and fewest amygdales and country rock xenoliths/xenocrysts. For fragmental deposits, we chose the largest, least altered pyroclastic bombs, and the most coherent, highly welded, spatter.

Samples selected for XRF determination of major and trace-element compositions of the groundmass were analysed at the laboratory of the Geological Survey of Canada (Ottawa, Ontario), courtesy of Bruce Kjarsgaard. First, samples were coarsely crushed and hand separated to exclude wall-rock clasts, alteration domains along fractures, large phenocrysts (or xenocrysts) and amygdales; despite these efforts, it was impossible to completely avoid contamination. Samples were then pulverized using an agate mill and analysed for major and trace elements by X-ray fluorescence (XRF).

Analyses of clinopyroxenes, olivine, and oxides were performed at the Victoria University of Wellington using a JEOL JXA-8230 superprobe equipped with five WDS spectrometers and one EDS. Operating conditions for minerals were 15 kV accelerating voltage, 12 nA beam current, focused beam with a spot size of 5 μm and 210 s counting time on peak position. The standard specimens used for calibration were the Kakanui clinopyroxene for clinopyroxene and olivine analyses, and an ilmenite for the oxides.

Trace and rare-earth elements (REE) in clinopyroxenes and phlogopite were analysed at the Centre for Trace Element Analysis, at Otago University, by laser ablation inductively coupled mass spectrometer (LA-ICP-MS), using a Resonetics RESOlution M-50-LR 193 nm excimer laser ablation system coupled to an Agilent 7500 cs/ce Quadrupole ICP mass spectrometer. Data were acquired making 500 μm transects on megacrysts, or 75 μm spot for smaller crystals; ablation lasts for 60 s at 5 Hz with a fluence of 2.5 J/cm^2. All runs used a mixture of Ar and He as a carrier gas. A rapid pre-analysis ablation was performed before each transect to clean the analysed surface. Major element compositions of the phlogopite were also acquired with LA-ICP-MS.

Petrography and XRF groundmass geochemistry

Each of the studied samples has phenocrysts within a microcrystalline groundmass. Residual glass is nowhere preserved. Rocks from the Northwest system display an inequigranular texture (Fig. 3) with crystals of clinopyroxene (from < 1 mm to up to 5 cm) and minor phlogopite in a groundmass of clinopyroxene and spinel microlites (< 0.1 mm). Rocks from the Southern system are nearly equigranular with microphenocrysts (< 1 mm) of clinopyroxene and minor olivine, in a groundmass of spinel and clinopyroxene microlites (< 0.1 mm). Common glomerocrystic (< 2 mm) aggregates of clinopyroxene and oxides with subordinate analcime and olivine are ubiquitous across the complex. Groundmasses of dike and sill samples are more coarsely crystalline (holocrystalline to hypocrystalline) than the volcaniclastic ones (hypocrystalline to glassy-cryptocrystalline), which have scattered microvesicles filled with secondary carbonate ± zeolite phases.

The petrography of Jagged Rocks products is consistent with that of other Hopi Buttes volcanoes (Williams 1936; Wenrich and Mascarenas 1982; Vazquez 1998; Hooten 1999; Lefebvre 2013). The rocks are classified as monchiquite, a feldspar-free alkaline lamprophyre bearing clinopyroxene and mica, and basanite, composed exclusively of clinopyroxene, olivine, and opaque oxides (Streckeisen 1978; Woolley et al. 1996; Le Maitre et al. 2002). Lamprophyres are products of water-rich magmas (Wimmenauer 1973; Rock 1991) and volatile-rich conditions are essential to stabilise the hydrous phases.

The groundmass compositions of these rocks (volatile-free normalized) plot within the basanite–tephrite field of TAS (Fig. 4a; after Le Bas et al. 1986). The analyses (Table 1) display strong silica undersaturation (SiO_2 37.8–43.9 wt%) over a wide range of MgO content (4.8–8.7 wt%) and moderate degrees of evolution (Mg# 57.4–48.1), coupled with low Cr and Ni concentrations (109–253 and 77–160 ppm, respectively). These rocks have affinities with the sodic alkaline series, displaying $NaO + K_2O/Al_2O_3 < 1$ and $Na_2O/K_2O > 1$ (Fig. 4b). From the geochemical classification of nephelinitic rock (Le Bas 1989), based upon the CIPW normative Ne and Ab, most of the samples plot in the field of melanephelinite and basanite/tephrite (Fig. 4c) ranging between 10–20% normative Ne and 0–12% of normative Ab.

Chondrite-normalized rare-earth (REE) and trace (TE) elements (Fig. 5) reveal trends very similar to those of other Hopi Buttes volcanoes (Suda et al. 1982; Alibert et al. 1986). Trace element composition is consistent with an intraplate setting (Alibert et al. 1986), and additional enrichment in Nb, Ta, Th, and U, geochemical tracers of alkaline magma can be ascribed to a metasomatized-mantle source (Pilet et al. 2002). There is strong fractionation between light- and heavy-REE, consistent with partial melting of a garnet-bearing source. Experiments with lamprophyres and other alkaline magmas have, however, failed to reproduce a near-liquidus assemblage from either anhydrous or hydrous garnet-bearing lherzolite at pressures lower than 40 kbar, instead suggesting partial melting of a hydrous phlogopite-bearing (olivine-) pyroxenite upper mantle source (Barton and Hamilton 1979; Esperança and Halloway 1987).

Mineral textures and major element geochemistry

Clinopyroxene

Clinopyroxene crystals in the studied rocks belong to the diopside and augite groups (Wo % 39.52–55.50; En %

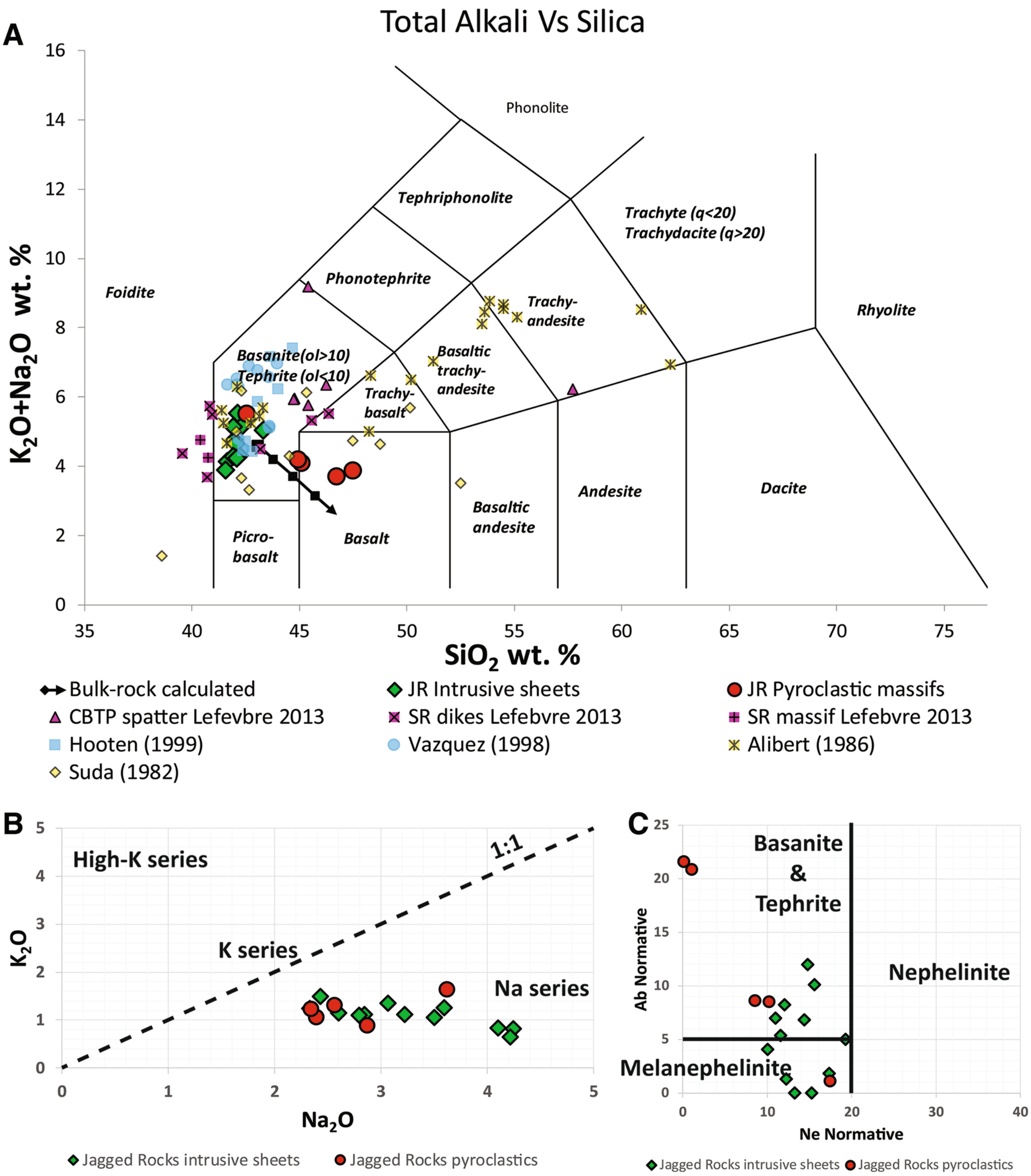

Fig. 4 Classification diagrams. **a** Total Alkali vs Silica (after Le Bas et al. 1986) plots of Jagged Rocks Complex groundmass, and some other Hopi Buttes whole-rock compositions, indicate alkaline series magmas. Jagged Rocks' bulk-rock composition (dark arrow) has been calculated by adding to the groundmass composition increasing proportion (marked by the arrow direction) of clinopyroxene type 1 core. Jagged Rocks pyroclastics (red circles) plot within the field of basalt, probably because the contamination of country rock clasts dispersed within the spatter. **b** Plot of Na2O Vs K2O discriminates among K- and Na-series. **c** Nephelinite classification diagram (after Le Bas 1989) plots also melanephelinite and tephrite fields; only the samples from Massif 3 display 23% of normative Ab and none show normative Ne, probably because there is a significant contamination from the quartz- and clay-rich sedimentary hosts

49.61–30.81; Fe % 10.88–13.69; after Morimoto et al. 1988). They display distinctive textures and growth zonations (Fig. 6) and a range of compositions (Fig. 7). Based upon textural features, we identified four classes of clinopyroxene, whose abundances differ in the different sectors of the complex.

Type 1 (Table 2; Fig. 6a–c) are coarse (up to 5 cm) and round clinopyroxene megacrysts that are a notable feature of the Northwest system at outcrop scale (Fig. 3). They consist of subhedral-to-anhedral cores with embayments and smooth outlines, which range in size from several mm up to few cm, surrounded by thin isopachous, subhedral-to-euhedral rims.

Table 1 XRF groundmass composition of Jagged Rocks Complex intrusive and pyroclastic deposits

Locality and rock type	NW dike close to Massif 1	TB$_J$ from western end of Massif 1	TB$_J$ from Massif 2	TB$_L$ from Massif 3	Coherent bomb from LTm deposit of Massif 3	Juvenile lapilli from LTm of Massif 5	Dike segment close to Massif 5	NEIS western end	NEIS western end: top layer	NEIS western end: inner layer	Central dike eastern end	South sill	Central dike western end	SW dike eastern end	SW dike western end	SIS	NEIS eastern end	Average	
Sample ID	KIA12-JAG1	KIA12-JAG2	KIA12-JAG3	KIA12-JAG4	KIA12-JAG5	KIA12-JAG6	KIA12-JAG7	KIA12-JAG8	KIA12-JAG8a	KIA12-JAG8b	KIA12-JAG9	KIA12-JAG11	KIA12-JAG12	KIA12-JAG13	KIA12-JAG15	KIA12-JAG16	KIA12-JAG17		
Major elements (wt%)																			
SiO_2	39.06	40.74	41.55	43.66	43.98	41.53	37.81	38.96	39.44	38.64	39.82	38.22	39.73	39.37	39.23	38.60	38.73	39.95	1.79
TiO_2	3.42	3.41	3.40	3.45	3.43	3.51	3.37	3.60	3.70	3.54	3.65	3.56	3.62	3.51	3.50	3.49	3.54	3.51	0.09
Al_2O_3	10.79	11.23	11.12	11.67	11.56	11.44	10.56	11.29	11.55	11.14	11.55	11.20	11.43	11.55	11.48	11.13	11.32	11.29	0.29
Cr_2O_3	0.04	0.04	0.04	0.04	0.04	0.04	0.04	0.02	0.02	0.02	0.02	0.02	0.02	0.02	0.02	0.02	0.02	0.03	0.01
Fe_2O_{3tot}	12.69	12.82	10.25	11.41	10.75	10.87	11.96	13.19	13.10	12.71	13.89	13.86	14.01	13.81	9.85	13.43	13.11	12.45	1.35
MnO	0.35	0.33	0.19	0.17	0.17	0.21	0.35	0.27	0.35	0.43	0.24	0.26	0.32	0.36	0.41	0.30	0.31	0.30	0.08
MgO	7.61	8.72	5.68	5.78	5.58	5.47	5.60	7.35	6.71	6.44	7.49	7.10	8.12	7.75	4.88	6.86	6.96	6.71	1.08
CaO	13.35	11.80	14.75	12.39	12.13	14.03	16.02	12.01	11.11	12.06	10.84	12.43	10.98	11.18	14.85	12.64	12.50	12.65	1.49
Na_2O	3.06	3.62	2.87	2.39	2.34	2.56	2.60	2.84	4.10	4.24	4.21	2.33	3.59	3.22	3.50	2.43	2.79	3.10	0.67
K_2O	1.35	1.64	0.88	1.06	1.23	1.30	1.15	1.12	0.83	0.82	0.64	1.24	1.26	1.12	1.06	1.49	1.10	1.13	0.25
P_2O_5	1.34	1.38	1.36	1.33	1.38	1.37	1.31	1.65	1.73	1.65	1.68	1.67	1.67	1.76	1.75	1.64	1.65	1.55	0.17
LOI	6.40	3.60	7.40	6.10	6.80	7.10	8.60	7.00	6.30	7.50	5.40	7.30	4.60	5.50	8.80	7.10	7.30	6.64	1.32
Sum	99.47	99.35	99.49	99.45	99.41	99.48	99.42	99.34	98.97	99.16	99.44	99.17	99.38	99.17	99.33	99.09	99.29	99.32	0.15
Mg# (FeO tot)	54.30	57.40	52.33	50.09	50.70	49.92	48.12	52.47	50.37	50.09	51.65	50.37	53.45	52.65	49.53	50.30	51.26	51.47	2.18
CIPW (wt%)																			
Quartz	0.00	0.00	0.00	0.00	0.00	0.00	0.00	0.00	0.00	0.00	0.00	0.00	0.00	0.00	0.00	0.00	0.00	0.00	0.00
Anorthite	12.50	9.83	16.06	19.19	18.62	17.16	15.02	15.90	11.30	9.54	11.30	17.81	11.86	14.55	13.60	15.78	16.34	14.49	3.01
Albite	0.00	1.10	8.49	20.84	21.56	8.59	0.00	6.95	10.07	5.00	11.98	4.05	6.79	8.24	1.83	1.30	5.35	7.18	6.38
Orthoclase	4.85	10.68	6.10	7.26	8.57	8.77	0.00	7.72	5.91	5.92	4.54	8.56	8.45	7.68	7.53	11.11	7.61	7.13	2.56
Nepheline	15.22	16.90	9.80	0.55	0.00	8.17	13.25	10.48	14.99	18.67	14.26	9.54	13.87	11.45	16.85	11.50	11.13	11.57	5.14
Leucite	3.33	0.00	0.00	0.00	0.00	0.00	6.33	0.00	0.00	0.00	0.00	0.00	0.00	0.00	0.00	0.00	0.00	0.57	1.69
Diopside	41.15	35.11	44.66	31.39	30.73	40.56	45.37	31.24	31.25	37.47	28.81	32.13	28.78	27.84	46.05	34.45	33.41	35.32	6.10
Hypersthene	0.00	0.00	0.00	0.00	1.46	0.00	0.00	0.00	0.00	0.00	0.00	0.00	0.00	0.00	0.00	0.00	0.00	0.09	0.35
Wollastonite	0.00	0.00	0.00	0.00	0.00	0.00	0.00	0.00	0.00	0.00	0.00	0.00	0.00	0.00	0.00	0.00	0.00	0.00	0.00
Olivine	10.03	13.73	2.33	8.11	6.35	3.83	4.24	13.41	11.88	9.26	14.76	13.46	16.07	15.95	0.20	11.76	11.97	9.84	4.91
Larnite	0.00	0.00	0.00	0.00	0.00	0.00	2.87	0.00	0.00	0.00	0.00	0.00	0.00	0.00	0.00	0.00	0.00	0.17	0.70
Ilmenite	7.05	6.83	7.07	7.08	7.09	7.28	7.12	7.48	7.64	7.39	7.45	7.43	7.33	7.19	7.39	7.26	7.38	7.26	0.20

Table 1 (continued)

Locality and rock type	NW dike close to Massif 1	TB$_J$ from western end of Massif 1	TB$_J$ from Massif 2	TB$_L$ from Massif 3	Coherent bomb from LTm deposit of Massif 3	Juvenile lapilli from LTm of Massif 5	Dike segment close to Massif 5	NEIS western end	NEIS western end: top layer	NEIS western end: inner layer	Central dike eastern end	South sill	Central dike western end	SW dike eastern end	SW dike western end	SIS	NEIS eastern end	Average	
Sample ID	KIA12-JAG1	KIA12-JAG2	KIA12-JAG3	KIA12-JAG4	KIA12-JAG5	KIA12-JAG6	KIA12-JAG7	KIA12-JAG8	KIA12-JAG8a	KIA12-JAG8b	KIA12-JAG9	KIA12-JAG11	KIA12-JAG12	KIA12-JAG13	KIA12-JAG15	KIA12-JAG16	KIA12-JAG17		
Magnetite	2.40	2.35	1.95	2.15	2.04	2.07	2.31	2.51	2.48	2.43	2.60	2.65	2.60	2.59	1.91	2.56	2.50	2.36	0.25
Apatite	3.37	3.37	3.45	3.33	3.48	3.47	3.37	4.18	4.36	4.20	4.19	4.25	4.13	4.40	4.51	4.16	4.19	3.91	0.44
Zircon	0.09	0.09	0.09	0.09	0.09	0.10	0.09	0.11	0.11	0.11	0.11	0.11	0.11	0.12	0.12	0.11	0.12	0.10	0.01
Chromite	0.01	0.01	0.01	0.01	0.01	0.01	0.01	0.00	0.00	0.00	0.00	0.00	0.00	0.00	0.00	0.00	0.00	0.00	0.00
Trace elements (ppm)																			
Cs	0.70	1.40	1.10	4.60	2.20	1.70	0.90	2.10	14.70	13.90	15.80	0.90	0.70	0.80	1.30	0.80	0.40	3.76	5.36
Sr	1628.40	2470.00	1508.10	1560.10	1622.60	1543.70	1884.30	2107.90	5215.10	3690.80	1450.70	3523.50	1847.80	3503.00	2076.50	2345.60	2738.80	2395.11	1039.47
Be	4.00	3.00	1.00	2.00	<1	5.00	2.00	1.00	2.00	5.00	3.00	6.00	2.00	5.00	<1	2.00	2.00	3.00	1.60
K	5603.50	6807.21	3652.65	4399.78	5105.41	5395.96	4773.35	4648.83	3445.11	3403.61	2656.47	5146.92	5229.93	4648.83	4399.78	6184.60	4565.81	4709.87	1040.60
Rb	34.40	31.90	23.20	24.60	29.40	33.00	29.50	27.80	20.80	19.40	18.10	28.30	34.90	29.80	31.10	27.50	26.60	27.66	5.03
Ba	1002.00	1087.00	909.00	1126.00	1495.00	852.00	1157.00	1070.00	1313.00	1335.00	1078.00	1151.00	1163.00	1256.00	1239.00	3280.00	1075.00	1269.88	540.97
Pb	7.00	8.00	8.00	8.00	9.00	8.00	8.00	10.00	9.00	10.00	8.00	10.00	9.00	10.00	9.00	9.00	9.00	8.76	0.90
Th	11.80	11.90	11.60	11.00	12.30	12.00	12.40	13.90	14.70	13.30	13.70	13.80	14.00	16.10	16.40	13.40	14.70	13.35	1.55
U	3.00	3.30	3.60	3.50	3.40	5.30	3.20	3.80	3.90	3.90	3.80	3.60	4.10	4.00	4.90	3.80	3.30	3.79	0.58
Nb	95.30	101.10	95.20	90.70	95.00	103.70	93.90	120.10	123.10	114.10	117.60	115.30	121.40	130.50	125.30	117.90	122.90	110.77	13.21
Ta	5.80	5.90	5.40	5.40	6.10	6.20	5.40	7.00	7.50	6.90	6.70	6.70	7.20	7.50	7.10	6.90	7.30	6.53	0.74
La	95.00	101.50	95.10	96.60	99.60	105.40	95.40	115.50	116.80	113.40	111.80	112.40	117.90	132.40	130.40	114.50	115.70	109.96	11.65
Ce	186.90	195.10	179.60	189.60	189.60	201.60	180.60	218.10	229.10	211.90	221.10	214.40	224.00	251.10	239.30	220.70	222.40	210.30	20.97
Pr	22.15	22.86	21.58	22.28	23.07	23.56	21.74	26.32	26.97	25.55	26.35	25.77	26.08	29.47	28.94	25.75	27.20	25.04	2.48
Nd	86.20	93.10	82.70	88.80	92.90	93.90	86.50	105.30	106.10	104.00	104.70	103.20	104.80	115.10	110.10	102.10	102.80	98.96	9.33
Zr	410.20	433.10	404.20	409.60	427.40	442.90	408.60	506.60	521.40	483.60	513.20	501.60	512.50	555.60	549.80	499.80	523.10	476.66	52.87
Hf	9.20	9.40	9.40	9.30	9.50	10.10	9.10	10.90	11.60	10.70	11.50	11.00	11.20	12.40	11.80	10.90	11.20	10.54	1.05
Sm	14.85	15.77	14.35	15.62	16.12	16.28	15.02	17.89	18.20	17.85	18.00	17.80	17.62	19.01	18.21	17.50	17.91	16.94	1.41
Eu	4.40	4.67	4.36	4.59	4.74	4.86	4.43	5.35	5.26	5.30	5.51	5.28	5.40	5.71	5.59	5.10	5.30	5.05	0.44
Gd	12.27	12.63	12.40	12.45	13.64	13.03	12.19	14.33	15.25	14.72	14.68	14.18	14.47	15.34	15.40	14.33	14.10	13.85	1.13
Tb	1.50	1.54	1.51	1.58	1.65	1.62	1.52	1.79	1.84	1.79	1.77	1.79	1.78	1.89	1.89	1.77	1.76	1.71	0.14
Ga	19.40	20.00	19.10	20.90	21.10	20.30	19.20	22.60	22.20	21.80	22.40	20.50	22.10	22.30	23.30	20.20	21.30	21.10	1.29
Ti	20,503.14	20443.18	20,383.23	20,682.99	20,563.09	21042.69	20,203.38	21,582.25	22,181.75	21,222.54	21,882.00	21,342.44	21,702.15	21,042.69	20,982.74	20,922.79	21222.54	21,053.27	561.68
V	227.00	230.00	228.00	226.00	236.00	234.00	222.00	216.00	220.00	211.00	224.00	218.00	228.00	220.00	220.00	218.00	217.00	223.24	6.71
Sc	21.00	21.00	20.00	21.00	21.00	20.00	20.00	19.00	19.00	18.00	19.00	19.00	19.00	18.00	17.00	18.00	18.00	19.29	1.26
Dy	7.16	7.40	7.07	7.40	8.11	7.70	7.08	8.20	8.55	8.27	8.35	8.21	8.90	9.51	9.15	8.52	8.66	8.13	0.74
Ho	1.14	1.18	1.09	1.25	1.20	1.31	1.16	1.18	1.28	1.23	1.32	1.37	1.31	1.44	1.38	1.29	1.31	1.26	0.09

Table 1 (continued)

Locality and rock type	NW dike close to Massif 1	TB_J from western end of Massif 1	TB_J from Massif 2	TB_L from Massif 3	Coherent bomb from LTm deposit of Massif 3	Juvenile lapilli from LTm of Massif 5	Dike segment close to Massif 5	NEIS western end	NEIS western end: top layer	NEIS western end: inner layer	Central dike eastern end	South sill	Central dike western end	SW dike eastern end	SW dike western end	SIS	NEIS eastern end	Average	
Sample ID	KIA12-JAG1	KIA12-JAG2	KIA12-JAG3	KIA12-JAG4	KIA12-JAG5	KIA12-JAG6	KIA12-JAG7	KIA12-JAG8	KIA12-JAG8a	KIA12-JAG8b	KIA12-JAG9	KIA12-JAG11	KIA12-JAG12	KIA12-JAG13	KIA12-JAG15	KIA12-JAG16	KIA12-JAG17		
Er	2.77	2.90	2.61	3.07	3.21	2.80	2.72	3.14	3.31	3.04	3.02	3.07	3.17	3.44	3.25	3.04	3.19	3.04	0.22
Tm	0.34	0.36	0.34	0.39	0.39	0.37	0.32	0.44	0.42	0.41	0.38	0.39	0.41	0.41	0.42	0.40	0.39	0.39	0.03
Y	30.50	32.50	29.80	32.50	33.30	33.00	29.90	35.70	38.60	34.30	35.80	35.00	36.30	39.10	37.90	36.40	36.10	34.51	2.89
Yb	1.84	2.09	2.06	2.21	2.30	2.28	2.06	2.36	2.28	2.34	2.30	2.20	2.52	2.54	2.41	2.33	2.40	2.27	0.18
Lu	0.27	0.28	0.27	0.29	0.31	0.28	0.22	0.31	0.33	0.32	0.31	0.31	0.31	0.34	0.32	0.29	0.34	0.30	0.03
Cr	253.15	246.31	246.31	253.15	253.15	253.15	246.31	116.31	116.31	109.47	157.37	136.84	143.68	130.00	130.00	136.84	123.16	179.50	61.98
Co	46.50	46.50	42.10	43.60	40.50	38.50	47.20	43.00	43.80	43.20	45.10	43.50	44.00	42.90	47.30	40.00	43.00	43.57	2.48
Ni	164.00	169.00	145.00	103.00	89.00	80.00	170.00	81.00	88.00	87.00	103.00	98.00	96.00	95.00	88.00	77.00	92.00	107.35	32.46
Cu	61.00	57.00	59.00	62.00	63.00	60.00	59.00	220.00	50.00	46.00	60.00	57.00	56.00	57.00	56.00	59.00	56.00	66.94	39.66
Zn	142.00	145.00	141.00	145.00	151.00	149.00	143.00	158.00	165.00	159.00	161.00	161.00	162.00	167.00	167.00	156.00	159.00	154.76	9.05
Mn	2710.62	2555.72	1471.48	1316.59	1316.59	1626.37	2710.62	2091.05	2710.62	3330.19	1858.71	2013.60	2478.28	2788.06	3175.29	2323.39	2400.83	2286.94	616.00
Sn	2.00	3.00	2.00	2.00	3.00	2.00	2.00	3.00	3.00	3.00	3.00	3.00	3.00	3.00	3.00	3.00	3.00	2.71	0.47
Mo	5.00	5.00	5.00	10.00	6.00	5.00	3.00	8.00	3.00	1.00	3.00	6.00	6.00	8.00	6.00	2.00	3.00	5.00	2.35
W	1.30	1.40	0.90	0.80	1.40	1.60	0.90	2.00	0.90	0.80	0.50	0.80	1.40	1.10	2.10	0.70	0.90	1.15	0.45

TB_J Juvenile dominated tuff breccia, *TB_L* Lithic and juvenile dominated tuff breccia, *LTm* Non-layered (massive) lapilli tuff, *NEIS* North east inclined sheet, *SIS* South inclined sheet (Acronym are from Re et al. (2015, 2016))

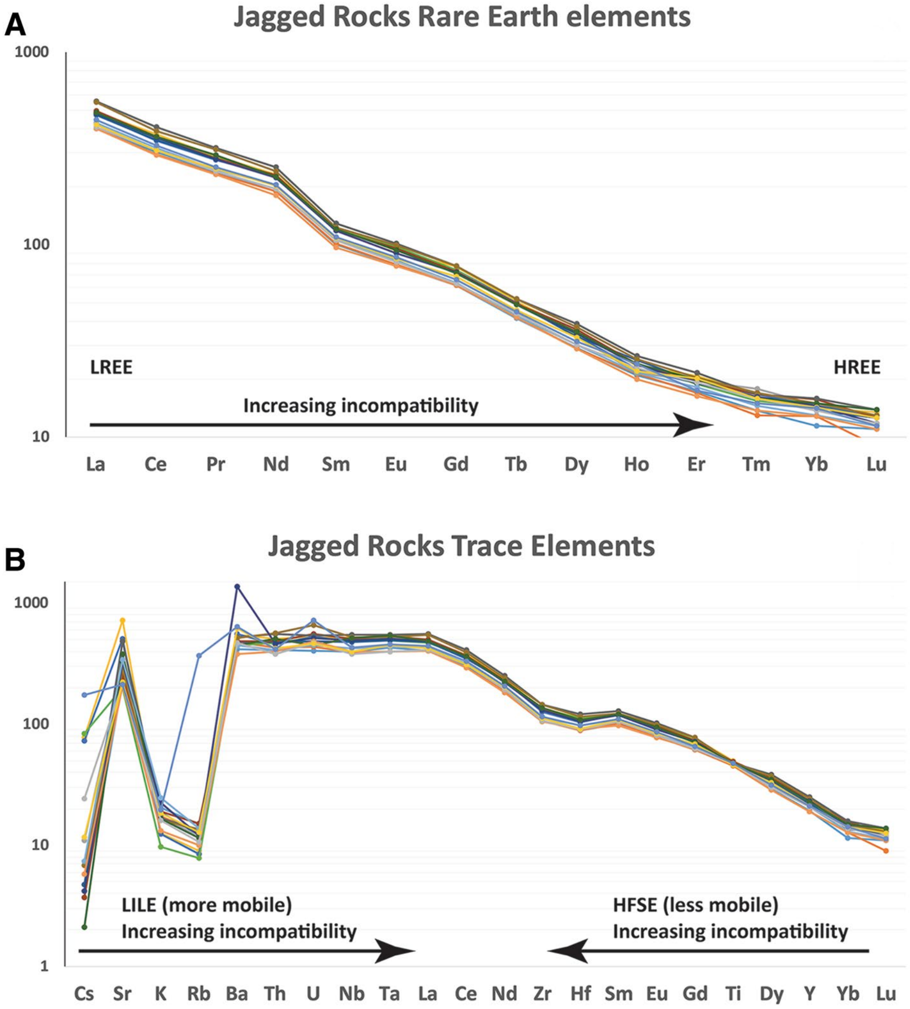

Fig. 5 Spider diagrams of REE (**a**) and TE (**b**) elements for the groundmass analyses. Jagged Rocks samples show depletion in heavy-REE relative to light ones and high concentration of elements as U, Th, Nb, and Ta markers of alkaline magma. Negative anomalies of K and Rb are also recorded in other analyses of Hopi Buttes volcanic rocks (e.g., Alibert et al. 1986)

The cores, pale to translucent in plane light, grade into broad mantling zones with a diffuse sieved texture. The sieved zones consist of areas pervaded by hollows and fractures, and in some specimens, the cores themselves display the sieved texture. Sharp optical boundaries separate the mantling zones from the outer rims, which have a pale-brownish shade and euhedral habit. Cores have very homogeneous major element compositions that cluster in a narrow interval (Mg# 77.6–85; SiO_2 48.9–53.3; TiO_2 0.6–2.1 wt%; FeO_{tot} 5.8–7.5 wt%; CaO 18.7–20.8 wt%; Na_2O 0.4–1.5 wt%), whereas rims have slightly evolved compositions (Mg# 74–77; SiO_2 45.2–47.9 wt%; TiO_2 2.6–3.8 wt%; FeO_{tot} 7.6–8.3 wt%; CaO 22–23.2 wt%; Na_2O 0.3–0.7 wt%). Mantling zone compositions are intermediate, overlapping those of cores and rims.

Type 2 (Table 2; Fig. 6f–h) are composite clinopyroxene crystals characterized by anhedral cores, with a green-to-pale-green shade under plane-polarized light, surrounded by euhedral pale rims. The green cores have angular to subround shapes with smooth outlines, which are pervaded by fractures, big hollows, and local domains with sieve textures. These crystals are only in the Northwest system. The green cores have distinct geochemical trends, which span a wide Mg# interval (64.3–80.6) at relatively constant SiO_2 (48.6–51.3 wt%) and TiO_2 (1–1.5 wt%) contents, narrowly varying Al_2O_3 (4.8–7 wt%) and CaO (18.7–21.1 wt%), and FeO_{tot} (6.3–10.7 wt%) and Na_2O (1–2.6 wt%) that increase in direct proportion to the degree of evolution. Conversely, the rims surrounding the green cores have compositions consistent with type 1 clinopyroxene rims, and in particular the most inward rims plot close to type 1 cores (high SiO_2 and Mg#, low TiO_2, CaO, and FeO_{tot}), whereas the outer rims plot at more-evolved compositions (depletion in SiO_2, MgO, Na_2O; enrichment in TiO_2, CaO, FeO_{tot}, and Al_2O_3).

Type 3 (Table 2; Fig. 6d) are mm-size clinopyroxenes with a regular zonation and an undisturbed crystal-growth stratigraphy that consists of multiple euhedral rims surrounding mostly euhedral cores. They represent the main clinopyroxene species in the Southern system, whereas they have subordinate abundance in the Northwest system. These crystals reveal a compositional interval consistent with the trend of type 1 clinopyroxenes, and outermost rims display

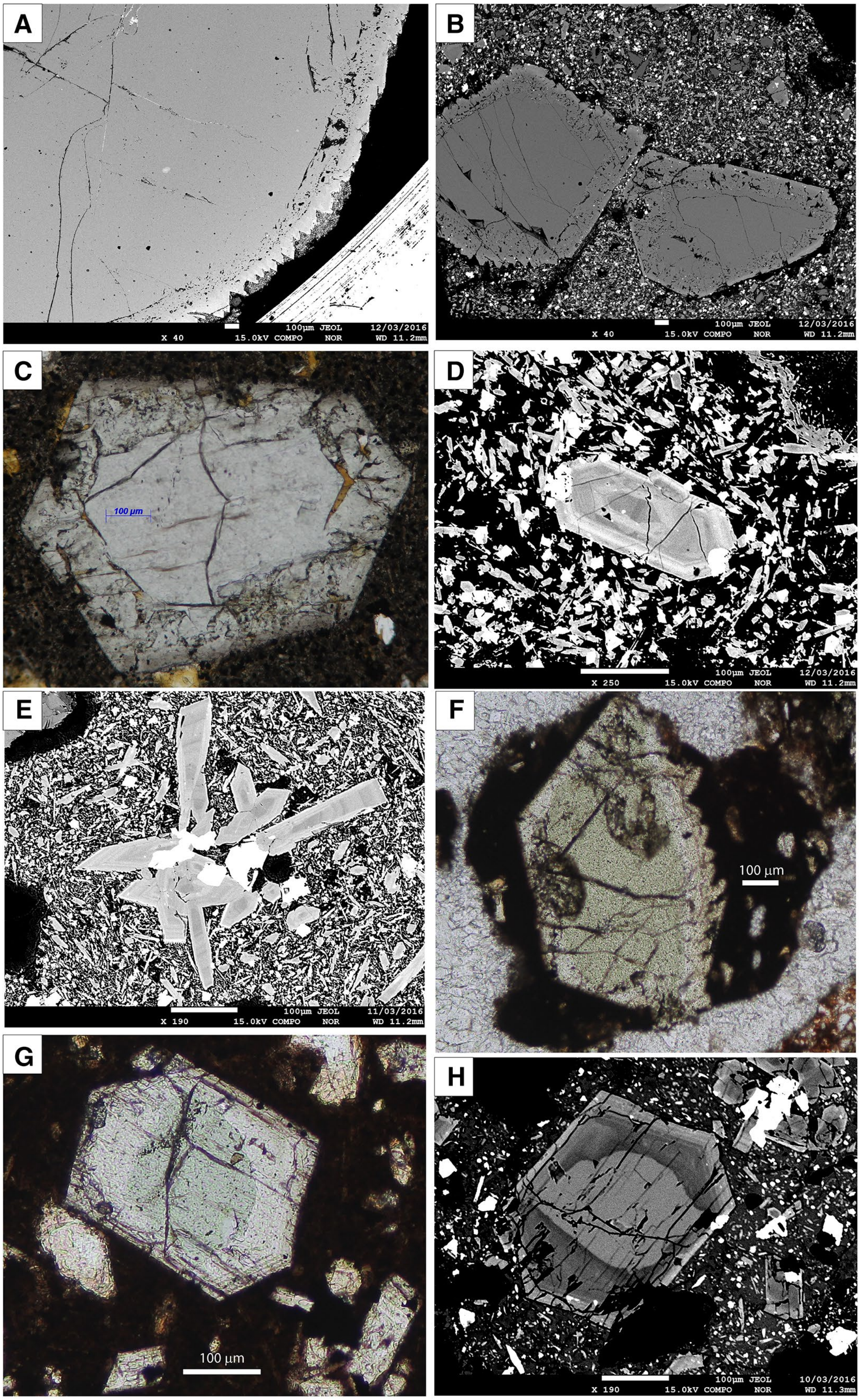
A
100µm JEOL 12/03/2016
X 40 15.0kV COMPO NOR WD 11.2mm
B
100µm JEOL 12/03/2016
X 40 15.0kV COMPO NOR WD 11.2mm
C
100 µm
D
100µm JEOL 12/03/2016
X 250 15.0kV COMPO NOR WD 11.2mm
E
100µm JEOL 11/03/2016
X 190 15.0kV COMPO NOR WD 11.2mm
F
100 µm
G
100 µm
H
100µm JEOL 10/03/2016
X 190 15.0kV COMPO NOR WD 11.3mm

◂**Fig. 6** Photomicrographs and backscatter images of clinopyroxene textures. **a–c** Type 1 crystals have homogeneous cores surrounded by mantling zones with diffuse sieved textures and euhedral rims. **d** Backscatter image of type 3 clinopyroxene with an undisturbed crystal-growth stratigraphy consisting of mostly euhedral zones of more- and less-enriched compositions. **e** Glomerocrysts are aggregates of type 3 clinopyroxene and oxide crystals. **f–h** Type 2 clinopyroxenes have anhedral cores with smooth outlines surrounded by mostly euhedral rims. Microlites (type 4) are the main constituent of the groundmass in all the backscatter images

enrichment in TiO_2 and FeO_{tot} relative to cores, which are more primitive (low Mg#) and depleted in SiO_2. The mid-zones across the crystal stratigraphy show, however, compositional variability that swings from more-primitive to more-evolved compositions and widely overlaps compositions of cores and rims (Mg# 70.3–81.7; SiO_2 43.4–50.9 wt%; TiO_2 1.6–4.5 wt%; FeO_{tot} 5.9–8.6 wt%; CaO 22.2–23.4 wt%; Na_2O 0.4–0.6 wt%). Type 3 clinopyroxenes are the main constituent of (poly-) crystal clusters called glomerocrysts (Fig. 6e).

Type 4 (Table 2) are clinopyroxene microlites, which are the main constituent of the rock groundmasses across the whole complex (Fig. 6). They cover a broad spectrum of composition (e.g., Mg# 68.5–77.9; TiO_2 2.2–5.3 wt%; FeO_{tot} 7.1–9 wt%), but the majority are clustered together with the outer rims, having more-evolved compositions.

Phlogopite

Rare phlogopite (Fig. 8a; average composition in Table 3) is present in the Northwest dike and massifs as isolated megacrysts (up to 3 cm) or as inclusions in fractures cutting type 1 clinopyroxene cores. Tabular hexagonal dark brown crystals reveal subhedral habits and a perfect lamellar cleavage. Some phlogopite crystals have sharp euhedral margins, whereas others display smooth and rounded shapes. Qualitative major element compositions, acquired with LA-ICP-MS, are characterized by high MgO (15.34% ± 0.24), K_2O (10.09% ± 0.16), and TiO_2 (6.66% ± 0.09), with SiO_2 and Al_2O_3 contents of 38.43% ± 0.44 and 15.99% ± 0.24, respectively.

Olivine

Olivine is overall scarce, and is more abundant in the intrusions of the Southern system (Fig. 8b–d), while apparently absent in the Northwest system. Olivines in the Southern system appear as pale-to-yellowish microphenocrysts (< 0.2 mm), with euhedral habit. Bigger anhedral crystals are very rare, broken apart, and altered. Olivines are well separated from type 3 clinopyroxene crystals, except where clustered into glomerocrysts, and this may indicate a synchronous crystallization. Olivine crystals do not display zonation and have a narrow compositional range (average composition in Table 3; Fo % 81.3–79.8). These olivines are Ca and Mn-rich (CaO 0.2–0.5 wt%; MnO 0.2–0.3 wt%) and Ni-poor (NiO 0.05–0.2 wt%).

Fe–Ti oxides

Oxides (average composition in Table 3) are a ubiquitous constituent of the groundmass of all rocks across the complex. They are euhedral-to-subhedral crystals usually < 0.2 mm, and are often attached to or enclosed within the external rims of clinopyroxene. This feature suggests that oxides crystallized from magma during growth of the clinopyroxene rims. Oxide compositions cover a wide range of Cr_2O_3 abundance (0–11.1 wt%) with the majority < 2 wt%, and of TiO_2 (10.5–18.9 wt%), with the majority comprising between 14 and 17 wt%. Total FeO ranges from 63 to 75 wt% and MgO is from 2.9 and 8.2 wt%. They plot along the magnetite–ulvospinel (titano-magnetite) solid-solution on the ternary diagram TiO_2–FeO–Fe_2O_3 (Fig. 9); therefore, a conservative inference is that the fO_2 of the system was within the magnetite vs stability range (above the Wustite–Magnetite and below the Hematite–Magnetite buffers).

Rare-earth (REE) and trace (TE) element composition and modelling

Rare-earth and trace element compositions were determined for a set of samples representative of the Northwest system. In particular, type 1 and 2 clinopyroxene cores and rims (Table 2) and one crystal of phlogopite (Table 3) were analysed. In this section, we describe the patterns of incompatible elements in these minerals. Mineral compositions are successively paired with appropriate distribution coefficients (*D*) to develop a model that calculates the abundance of incompatible elements within the hypothetical melt in equilibrium with each mineral.

All clinopyroxene plots display similar shapes on REE and TE spider diagrams (Fig. 10). There is depletion in heavy-REE (HREE) relative to light ones (LREE), and TE display depletion in large-ion lithophile elements (LILE; Cs, K, Rb, Pb) relative to high field strength elements (HFSE), with very low abundances of the most-compatible trace elements, such as Cr, Co, Ni, Cu, Zn, and Mn, in clinopyroxene. There is a little evidence of partitioning between $V^{(3+;5+)}$ and $Sc^{(3+)}$ between cores (V/Sc ~ 5) and rims (V/Sc ~ 2), with the former decreasing (from ~ 230 to ~ 180 ppm) and the latter increasing (from ~ 50 to ~ 90 ppm) toward the rims. The transects performed over type 1 clinopyroxenes (Fig. 11) reveal that cores and mantling zones, which have the most primitive compositions (Mg# ~ 80), have the lowest

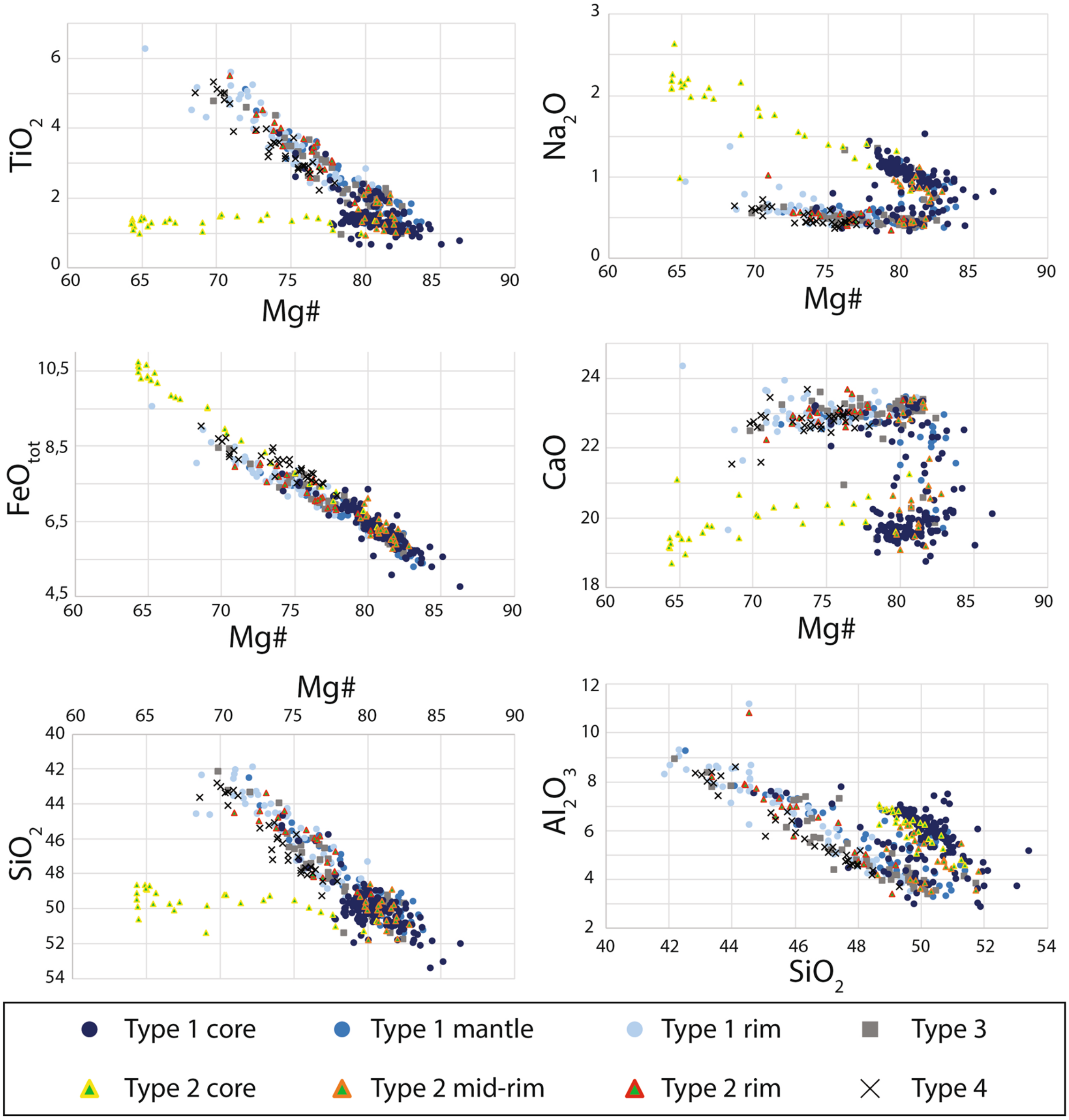

Fig. 7 Variation diagrams for clinopyroxene. Major oxides are plotted versus Mg#, except for Al_2O_3 plotted versus SiO_2. All the plots reveal two different arrangements, with the type 2 (green-) cores diverging from the main array

concentrations of incompatible elements, whereas the outermost rims, about 100 µm thick, are evolved and display ~ 5 times enrichment. Type 2 green cores, the most evolved cores (Mg# ~ 65), have higher REE and TE abundances compared to type 1 cores and are comparable with the rim compositions (Fig. 10). Phlogopite crystals have high concentrations of LILE cations, in particular Rb and K, and low abundances of REE and HFSE, with the exception of Nd, Zr, and in particular Ti, which have a strong positive anomaly.

The concentrations of incompatible elements for hypothetical melts in equilibrium with cores and rims of clinopyroxene types 1 and 2, and with the phlogopite, are calculated by pairing each incompatible element measured within the crystals with the appropriate partition coefficient controlling the distribution of that element between solid and liquid phases. The model, based upon the formulation $X^{\mathrm{TE}}_{\mathrm{melt}} = \frac{X^{\mathrm{TE}}_{\mathrm{xls}}}{D^{\mathrm{TE}}}$, assumes that partitioning of the elements is governed only by the fractionation between solid and liquid occurring during the crystallization process; the effects of temperature, pressure, fO_2, and melt composition on the partition coefficients are not considered. To minimize the effect of the melt composition, however, most of the clinopyroxene and phlogopite TE and REE were modelled with partition coefficients ($D^{\mathrm{TE}}_{\mathrm{xls/melt}}$) measured in an alkaline lamprophyre (Foley et al. 1996). For clinopyroxene, this set of partition coefficients is integrated with other

Table 2 Representative composition of studied clinopyroxene types

Major elements (wt%)	Type 1						Type 2						Type 3						Type 4	
	Average core	SD	Average mantle zone	SD	Average rim	SD	Average green core	SD	Average mid rim	SD	Average rim	SD	Average cores	SD	Average mid rim	SD	Average rim	SD	Average	SD
SiO_2	49.93	1.22	48.59	2.04	45.70	2.26	49.72	0.77	50.20	0.84	46.27	1.71	49.55	1.44	48.83	1.84	46.07	1.97	46.15	1.90
TiO_2	1.50	0.54	2.34	0.91	3.66	0.98	1.31	0.16	1.52	0.40	3.47	0.85	2.00	0.62	2.40	0.69	3.52	0.79	3.59	0.87
Al_2O_3	5.86	1.03	5.52	1.35	6.82	1.72	6.08	0.72	4.75	0.85	6.55	1.68	4.39	1.36	4.43	1.45	6.18	1.52	5.99	1.47
Cr_2O_3	0.26	0.15	0.19	0.24	0.02	0.04	0.07	0.12	0.34	0.27	0.01	0.02	0.08	0.11	0.01	0.01	0.01	0.01	0.01	0.01
FeO_{tot}	6.45	0.49	6.45	0.68	7.52	0.64	9.16	1.39	6.32	0.35	7.34	0.50	6.59	0.47	6.74	0.71	7.59	0.56	8.03	0.42
MnO	0.12	0.02	0.11	0.02	0.12	0.02	0.22	0.07	0.13	0.02	0.11	0.02	0.12	0.03	0.13	0.02	0.13	0.02	0.13	0.02
MgO	14.72	0.82	14.10	1.07	12.52	1.11	11.96	1.37	15.08	0.57	12.85	0.89	14.45	0.77	14.12	0.92	12.67	0.89	12.79	1.03
CaO	20.41	1.33	22.44	1.04	22.97	0.59	19.84	0.62	21.16	1.55	23.01	0.33	22.50	1.06	23.00	0.25	22.99	0.28	22.74	0.40
Na_2O	0.93	0.26	0.58	0.17	0.56	0.15	1.78	0.44	0.74	0.23	0.53	0.13	0.55	0.25	0.48	0.08	0.52	0.07	0.50	0.09
Total	100.42	0.71	100.65	0.44	100.34	0.56	100.56	0.37	100.52	0.53	100.58	0.85	100.51	0.44	100.48	0.35	100.04	0.44	100.37	0.51
Si	1.83	0.04	1.79	0.06	1.70	0.07	1.84	0.02	1.84	0.02	1.72	0.06	1.82	0.05	1.81	0.05	1.73	0.07	1.72	0.06
Ti	0.04	0.02	0.07	0.03	0.10	0.03	0.04	0.00	0.04	0.01	0.10	0.02	0.06	0.02	0.06	0.02	0.10	0.02	0.10	0.03
Al	0.25	0.04	0.24	0.06	0.30	0.08	0.26	0.03	0.20	0.04	0.29	0.07	0.20	0.06	0.19	0.05	0.26	0.07	0.26	0.07
Cr	0.01	0.00	0.01	0.01	0.00	0.00	0.00	0.00	0.01	0.01	0.00	0.00	0.00	0.00	0.00	0.00	0.00	0.00	0.00	0.00
Fe^{3+}	0.07	0.02	0.09	0.03	0.13	0.05	0.12	0.03	0.08	0.02	0.12	0.03	0.09	0.02	0.10	0.02	0.12	0.03	0.12	0.03
Fe^{2+}	0.13	0.02	0.11	0.01	0.11	0.04	0.17	0.03	0.12	0.02	0.11	0.03	0.12	0.02	0.11	0.01	0.11	0.02	0.13	0.03
Mn	0.00	0.00	0.00	0.00	0.00	0.00	0.01	0.00	0.00	0.00	0.00	0.00	0.00	0.00	0.00	0.00	0.00	0.00	0.00	0.00
Mg	0.80	0.04	0.77	0.05	0.70	0.06	0.66	0.07	0.82	0.03	0.71	0.05	0.79	0.04	0.78	0.04	0.71	0.05	0.71	0.05
Ca	0.80	0.06	0.89	0.04	0.92	0.02	0.79	0.02	0.83	0.06	0.92	0.02	0.89	0.05	0.91	0.01	0.92	0.01	0.91	0.02
Na	0.07	0.02	0.04	0.01	0.04	0.01	0.13	0.03	0.05	0.02	0.04	0.01	0.04	0.02	0.03	0.00	0.04	0.01	0.04	0.01
Mg# (Fe_{tot})	80.22	1.84	79.46	2.94	74.66	3.14	69.77	5.39	80.96	0.88	75.65	2.38	79.58	1.85	78.79	2.87	74.77	2.66	73.85	2.46
Wo %	45.55	2.83	46.11	3.67	47.53	2.22	46.93	2.81	47.49	1.94	48.17	1.95	47.93	2.19	48.41	1.97	49.02	3.46	47.40	2.46
En %	42.76	3.99	41.80	4.14	40.33	3.73	41.34	3.59	41.44	3.17	39.62	2.97	41.52	3.47	40.26	2.72	39.95	3.94	41.11	2.85
Fs %	11.68	2.03	12.09	2.51	12.14	2.42	11.73	2.04	11.07	1.60	12.21	1.44	10.55	2.26	11.32	1.60	11.03	3.06	11.49	1.11

Trace elements (ppm)	Average T1 core	SD	Average T1 rim	SD	Average T2 core	SD	Average T2 rim	SD
Cs	0.01	0.02	0.03	0.08	0.05	0.13	0.02	0.08
Sr	179.34	52.66	280.39	15.32	344.62	68.80	299.50	237.87
Li	2.87	2.85	2.50	1.71	3.36	1.05	2.06	0.74
Be	0.34	0.13	0.54	0.13	0.75	0.23	0.50	0.21
K	98.79	132.78	209.85	238.57	411.55	638.79	190.34	463.88
Rb	0.18	0.33	0.55	0.48	0.96	1.61	0.49	1.30

Table 2 (continued)

Trace elements (ppm)	Average T1 core	SD	Average T1 rim	SD	Average T2 core	SD	Average T2 rim	SD
Ba	4.34	8.15	30.94	93.91	15.64	25.11	11.72	23.41
Pb	0.32	0.52	0.32	0.30	0.35	0.25	0.28	0.42
Th	0.15	0.16	0.47	0.32	0.25	0.23	0.40	0.42
U	0.04	0.08	0.09	0.10	0.06	0.06	0.07	0.12
Nb	1.16	1.54	2.83	2.06	2.28	2.08	2.50	3.37
Ta	0.13	0.10	0.39	0.17	0.28	0.10	0.35	0.23
La	6.14	3.55	17.13	4.19	12.08	3.71	15.79	7.41
Ce	20.93	9.58	52.89	9.80	42.62	11.66	49.61	18.03
Pr	3.71	1.47	8.90	1.49	7.57	2.12	8.45	2.68
Nd	19.85	7.19	45.90	8.02	39.60	11.52	43.89	12.71
Zr	76.68	47.68	240.53	52.75	230.09	82.63	224.56	82.42
Hf	3.25	2.01	10.01	2.19	9.11	3.58	9.41	3.08
Sm	5.46	1.78	11.58	1.82	10.14	2.91	11.08	2.67
Eu	1.78	0.53	3.56	0.45	3.16	0.94	3.43	0.74
Gd	5.15	1.65	10.49	1.44	8.91	2.34	9.99	1.94
Tb	0.66	0.21	1.27	0.12	1.15	0.33	1.21	0.24
Ga	11.43	1.99	13.03	0.74	15.75	3.21	13.02	2.29
Ge	2.17	0.25	2.52	0.04	2.38	0.27	2.42	0.27
Ti	7862.90	3107.20	14242.16	2993.35	7899.57	1556.39	13,366.25	3473.43
V	234.56	49.51	175.40	23.26	207.29	40.45	175.02	27.89
Sc	50.22	20.75	89.74	19.17	45.82	17.44	83.62	18.47
Dy	3.54	1.04	6.45	0.78	6.00	1.58	6.24	1.21
Ho	0.56	0.16	1.02	0.12	0.96	0.28	0.98	0.18
Er	1.31	0.40	2.32	0.22	2.28	0.63	2.22	0.37
Tm	0.15	0.04	0.25	0.03	0.26	0.07	0.25	0.06
Y	13.82	3.94	24.62	2.87	23.44	6.53	23.85	4.45
Yb	0.82	0.23	1.42	0.17	1.45	0.43	1.36	0.26
Lu	0.10	0.03	0.20	0.01	0.19	0.06	0.19	0.04
Cr	1810.97	1031.23	579.93	259.07	226.33	397.84	763.77	1283.10
Co	37.17	1.89	35.19	0.63	30.74	4.63	35.31	1.46
Ni	254.73	70.73	142.27	14.22	62.80	66.78	146.24	47.13
Cu	4.29	8.55	4.70	2.63	2.65	4.91	3.35	3.37
Zn	44.37	6.50	43.86	2.38	83.61	31.64	45.64	9.49
Mn	969.89	136.79	881.77	100.63	1589.95	499.93	922.54	160.26
As	0.21	0.22	0.44	1.44	4.20	8.42	0.87	4.60

Table 2 (continued)

Calculated parameters	Average T1 core	SD	Average T1 mantle zone	SD	Average T1 rim	SD	Average T2 core	SD	Average T2 mid rim	SD	Average T2 rim	SD	Average T3 core	SD	Average T3 rim	SD	Average T4	SD
T (K)	1575.60	2.82	1538.36	26.03	1511.86	7.31	1595.50	5.80	1552.53	15.11	1498.10	19.49	1496.13	22.80	1502.05	15.43	1467.84	16.46
P (kbar)	14.27	0.27	11.00	2.28	8.01	0.94	17.31	0.54	12.24	1.28	6.19	2.23	6.30	2.71	6.69	1.76	2.34	1.98
Kd	0.29	0.0007	0.28	0.0062	0.28	0.0018	0.30	0.0014	0.29	0.0036	0.27	0.0048	0.27	0.0056	0.27	0.0038	0.26	0.0041
ΔDi-Hd	0.09	0.0068	0.12	0.0248	0.09	0.0253	0.13	0.0059	0.11	0.0180	0.06	0.0162	0.09	0.0271	0.07	0.0157	0.02	0.0135
H_2O^a	2.88	0.11	2.95	0.33	1.31	0.70	3.32	0.11	2.73	0.21	1.05	0.59	2.32	0.48	1.14	0.23	0.79	0.49

[a] H_2O values are estimated with the empirical geohygrometer of Armienti et al. (2013)

experimental measurements from alkali basalt (Hart and Dunn 1993), which closely agree with those for lamprophyre (Foley et al. 1996). The partition coefficient of V (D^V) is strongly dependent on the fO_2, and the one chosen (from Laubier et al. 2014) is referenced to the QFM buffer.

Modelling results reveal that all the hypothetical melt-calculated curves (Fig. 12) mimic the shape of the groundmass spider diagram, but at different concentrations. In particular, melts calculated from type 1 clinopyroxene cores closely match the concentrations in the groundmass, with negligible differences in Ba, Th, U, Nb, and Ta, whereas the melts calculated from green cores (type 2) and rims display ~ 7 times enrichment in incompatible elements compared to the groundmass. The hypothetical melt calculated from the phlogopite is overall comparable with the hypothetical melt calculated from the type 1 cores, thereby with the groundmass, with major differences for Th and Ce.

Clinopyroxene–melt geothermobarometer

Mineral-melt geothermobarometry was performed to estimate pressure and temperature of equilibria among solid and liquid phases. At Jagged Rocks, there coexist different sets of clinopyroxenes that were hosted in the magma, and all of them share a suite of geochemical features despite textural features indicating degrees of disequilibrium. For example, type 1 clinopyroxene cores display sieve textures that indicate disequilibrium, even though modelling of trace element concentrations indicates that their compositions are in equilibrium with a melt with the observed groundmass composition. On the other hand, type 1 rims, which have euhedral shapes and sharp margins, reveal a greater enrichment in incompatible elements (high REE, Ti, Al) than would be at equilibrium with a groundmass composition melt. We recognize that there are geochemical differences among the melts in equilibrium with crystal's cores and rims, but have cautiously applied the clinopyroxene–melt geothermobarometer (Putirka et al. 2003) using the groundmass composition as a single proxy for the liquid for all the sets of clinopyroxenes. We infer that this approximation is an acceptable simplification for the following reasons. (1) Groundmass analyses exclude the main mass of large crystals, because all oversize crystals were picked out from the coarsely crushed samples prior to powdering (see "Sampling and analytical methods" paragraph). (2) Residual glass, which could provide direct evidence of the melt's composition when emplaced, is nowhere preserved in the deposits. (3) We attempted to calculate alternative melt compositions (by adding and subtracting to the groundmass analyses different proportion of clinopyroxene, olivine, and phlogopite components), but no attempt produced a composition in a better equilibrium with the crystals than is the composition of the

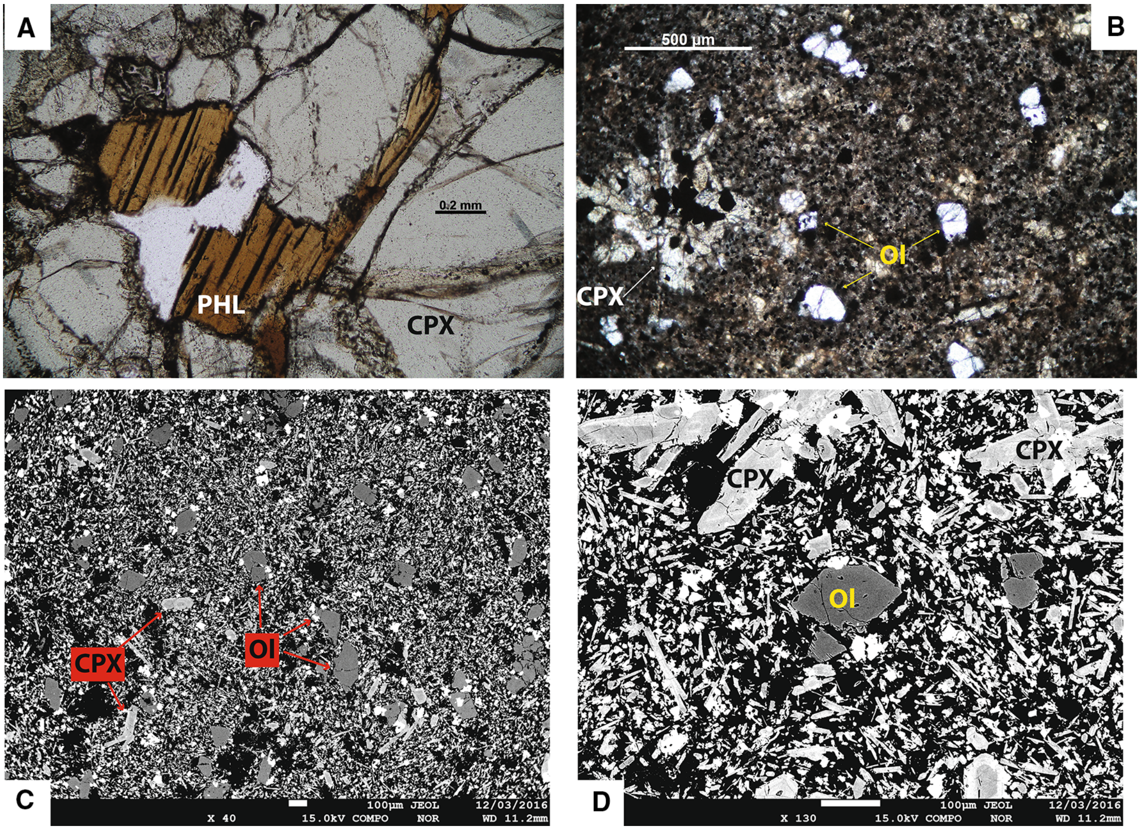

Fig. 8 Photomicrographs and backscatter images. **a** Phlogopite crystal (PHL) in plane-polarized light as inclusion within a type 1 clinopyroxene core (CPX). **b** Picture taken in plane-polarized light of the SW dike revealing some crystals of olivine (Ol) and a glomerocrysts of aggregated clinopyroxene and oxides. **c** Backscatter picture of SW dike sample, revealing microphenocrysts of olivine within a groundmass of clinopyroxene and oxides. **d** Backscatter picture of an inclined-sheet sample with euhedral crystals of olivine, two glomerocrysts of aggregated clinopyroxenes and oxides within a groundmass of the same mineral phases

groundmass. (4) In addition, the P–T trends obtained with these new alternative melts display equivalent correlations with the different clinopyroxene types. For these reasons, we infer that, although the quantitative results are affected by the uncertainties related to the approximation of the melt composition, the geothermobarometric computations performed have at least qualitative significance, because the P–T paths for the different classes of clinopyroxene are repeatable. To address how much each clinopyroxene–melt pair diverges from equilibrium, we calculated the equilibrium constant for Fe–Mg exchange between clinopyroxene and melt ($\mathrm{Kd}^{\mathrm{Fe-Mg}}_{\mathrm{cpx/melt}} = 0.27 \pm 0.03$; Putirka et al. 2003); the standard error estimate with this calibration is 1.7 kbar and 33 °C (Putirka et al. 2003). An additional test for equilibrium is performed by calculating the deviation between the (1) "predicted" and the (2) "measured" diopside–hedenbergite components of clinopyroxene (ΔDi-Hd; Mollo et al. 2013) for (1) clinopyroxene–melt pairs in equilibrium and (2) at the interior of the analysed crystal, respectively. The higher the ΔDi-Hd value, the greater is the error in the T and P estimation.

Figure 13 shows the P–T path obtained (results summarized in Table 2) and the plot of average values for Kd and ΔDi-Hd, which reveal that all the clinopyroxene–groundmass melt pairs are close to equilibrium. Type 2 green cores, which reveal the highest disequilibrium with the host melt (Kd ~ 0.296; ΔDi-Hd ~ 0.124), yield the highest pressures at about 17 kbar (~ 60 km). Type 1 cores equilibrated at about 14 kbar (~ 50 km), together with some of the mid-zone growth over the green cores. All the outermost rims display crystallization pressures between 8 and 5 kbar (~ 25 km), and the microlites, indicating pressure between 5 and 0.5 kbar (average of 2 kbar; ~ 7 km), represent the shallowest bit of crystallization.

Empirical clinopyroxene geohygrometer

We computed the equilibrium melt H_2O wt% with the empirical geohygrometer of Armienti et al. (2013), which

Table 3 Representative compositions of studied phlogopite, olivine, and Fe–Ti oxides

	Olivine			Fe–Ti oxide			Phlogopite	
	Average	SD		Average	SD		Average[a]	SD
SiO2	39.23	0.15	SiO_2	0.17	0.25	SiO_2	38.43	0.44
TiO_2	0.03	0.02	TiO_2	15.09	1.24	TiO_2	6.66	0.09
Al_2O_3	0.03	0.02	Al_2O_3	4.28	0.53	Al_2O_3	15.99	0.24
Cr_2O_3	0.02	0.02	Cr_2O_3	1.07	1.87	FeO_{tot}	8.83	0.14
FeO_{tot}	17.40	0.33	FeO_{tot}	71.53	2.02	MnO	0.04	0.00
MnO	0.30	0.03	MnO	0.52	0.11	MgO	15.34	0.24
MgO	42.74	0.27	MgO	6.00	0.77	CaO	0.08	0.02
CaO	0.29	0.08				Na_2O	0.69	0.05
Na_2O	0.14	0.06				K_2O	10.09	0.16
						P_2O_5	0.01	0.00
Total	100.19	0.44	Total	98.66	0.85	Total	96.16	1.38
Si	1.00	0.00	$Fe_2O_3^b$	35.64	2.71			
Ti	0.00	0.00	FeO^b	35.89	1.94	Li	1.28	0.12
Al	0.00	0.00				Be	0.13	0.03
Cr	0.00	0.00	Mg# (Fe^{2+})	22.98	3.08	K	84,063.30	1369.01
Fe^{3+}	0.01	0.01	Cr#	10.55	12.83	Sc	6.27	0.14
Fe^{2+}	0.36	0.01				Ti	39,951.72	512.96
Mn	0.01	0.00				V	382.91	6.58
Mg	1.62	0.01				Cr	1519.48	563.57
Ca	0.01	0.00				Mn	292.17	2.96
Na	0.00	0.00				Co	93.69	1.08
						Ni	958.13	14.11
Mg# (Fe_{tot})	81.41	0.34				Cu	13.33	10.19
						Zn	81.42	16.20
Te %	0.32	0.03				Ga	16.88	0.72
Fo %	80.83	0.33				Ge	0.73	0.17
Fa %	18.46	0.34				As	0.79	0.26
Ca–Ol %	0.39	0.10				Rb	269.65	12.89
						Sr	247.75	11.36
						Y	0.08	0.02
						Zr	10.09	0.25
						Nb	10.97	0.38
						Cs	1.39	0.05
						Ba	5083.35	202.27
						La	0.05	0.02
						Ce	0.10	0.06
						Pr	0.01	0.00
						Nd	0.03	0.02
						Sm	0.01	0.00
						Eu	0.12	0.01
						Gd	0.01	0.00
						Tb	0.00	0.00
						Dy	0.01	0.00
						Ho	0.00	0.00
						Er	0.00	0.00
						Tm	0.00	0.00
						Yb	0.01	0.00
						Lu	0.00	0.00
						Hf	0.30	0.03

Table 3 (continued)

Olivine		Fe–Ti oxide			Phlogopite	
Average	SD	Average	SD		Average[a]	SD
				Ta	0.63	0.02
				Pb	1.77	1.24
				Th	0.01	0.00
				U	0.00	0.00

[a] Major elements are qualitative data

[b] Calculated values

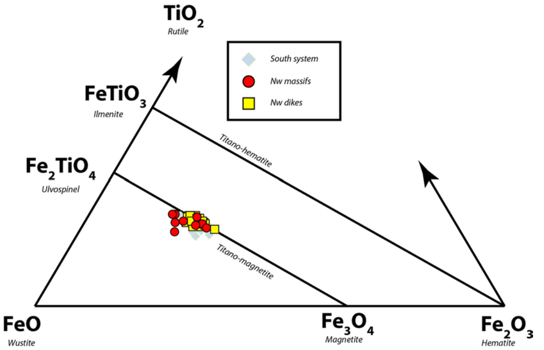

Fig. 9 Classification diagram for Fe–Ti oxide minerals. The compositions lie along the magnetite–ulvospinel solid-solution boundary

is related to pressure (GPa), temperature (°C), and clinopyroxene compositions expressed in terms of the components calculated with the formulation of Putirka et al. (2003). This model is calibrated for clinopyroxene compositions associated with experimental alkaline melts of Etna (trachybasalt and hawaiite compositions) at low pressure (1–8 kbar), with an average error of ± 0.5 wt% (Armienti et al. 2013). The calibration of this model lies somewhat beyond the system conditions during emplacement of the Jagged Rocks Complex, but the data presented by Armienti et al. (2013) still reveal good agreement at pressures up to 14 kbar.

The results (Table 2) indicate that melt-water content was highest during growth of clinopyroxene cores, about 3.5 wt% H_2O for the type 2 cores and about 3 wt% for the type 1, dropping to about 1 wt% for microlites (type 4) and crystal rims. These contents cannot be considered quantitatively accurate, although they are reasonable for an alkaline lamprophyre melt, but the implied melt-water decrease from cores to rims is consistent with progressive exsolution of water from the melt (represented by groundmass) at decreasing depths.

Discussion

At the Jagged Rocks Complex, different clinopyroxene populations coexisted in host magma(s) represented by the dikes, sills, and massifs. The clinopyroxenes have a range of different textures, compositions, and pressures at which they were at equilibrium with their host groundmass composition melt(s). This large diversity indicates a complex petrogenetic history that resulted from phases of growth, zonation, and resorption.

Major element geochemistry separates clinopyroxenes into two different groups. Clinopyroxene types 1, 3, and 4, together with type 2 rims, lie on a common geochemical trend that reveals a core-to-rim record of magma evolution, whereas type 2 (green-) cores exhibit differences in all major element behaviour and appear totally unrelated to the others (Fig. 7). On the other hand, TE and REE geochemistry (Fig. 10) shows consistent proportions of incompatible elements for all the clinopyroxene types, but at different concentrations. The enrichment in incompatible elements is directly proportional to the decrease in Mg#; type 1 cores have the highest Mg# and the lowest abundance of TE; in contrast, type 2 cores and all the rims have lower Mg# and higher TE concentration. Moreover, based upon the geochemistry of the calculated hypothetical melts (Fig. 12), type 1 cores, despite their sieved textures, and the phlogopite have a strong geochemical affinity with the groundmass proxy for the melt. This evidence suggests that a melt with a composition similar to the groundmass was in equilibrium the type 1 cores, whereas type 2 green cores are foreign xenocrysts that were incorporated at an early stage or at a great depth into the magma. The similarities highlighted by the TE compositions, however, point to a common mantle source. The rims of type 1 and 2 clinopyroxenes, which share similar thicknesses (~ 100 µm) and geochemistry, were grown onto their cores over the same time, during a later crystal-growth stage.

Fig. 10 Plots of the average trace (top plot) and Rare-earth (bottom plot) element compositions. In both the plots, the thick light blue line represents the groundmass, which is a proxy for the host melt, the black and the light grey lines are core and rim of type 1 clinopyroxene, and dark-green and light-green are core and rim of type 2 clinopyroxenes, respectively. Purple line in the trace elements plot is the phlogopite

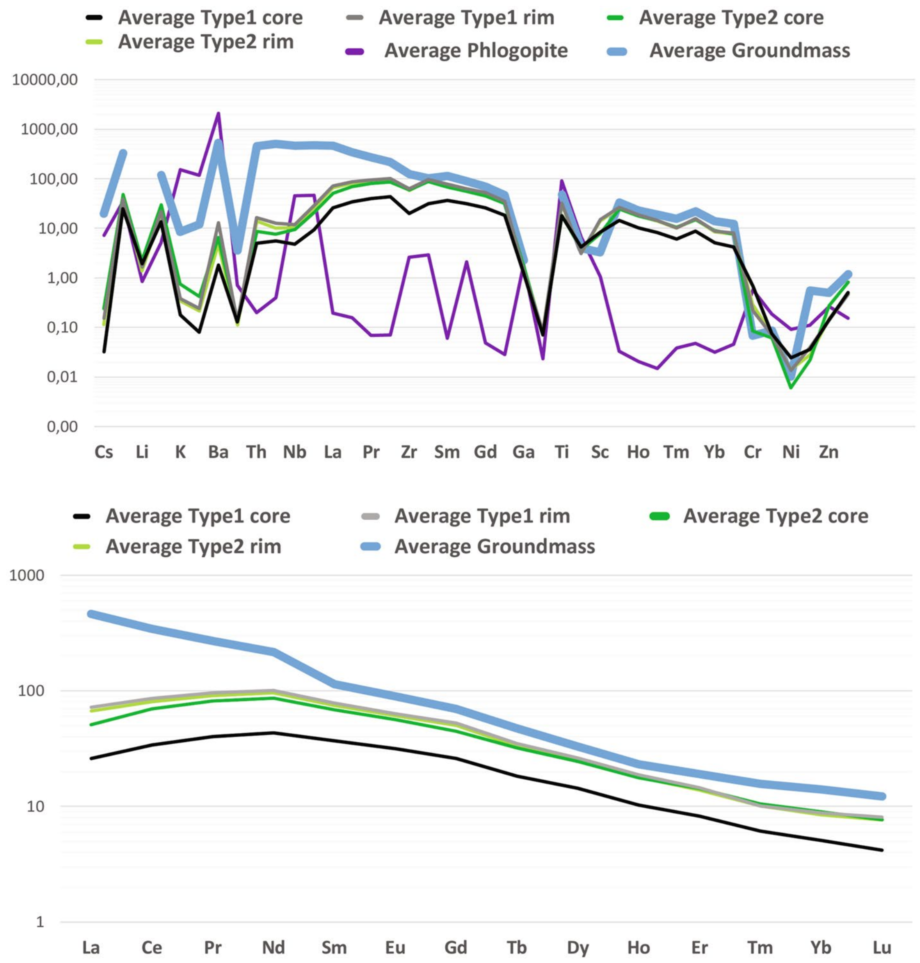

Sources of different clinopyroxene core populations

It is impossible to establish the source of the clinopyroxene cores from their geochemistry alone, and since lamprophyre magmas are known to host a variety of xenolith components, there is the possibility that these cores are igneous clinopyroxene “antecrysts” crystallized from different magma batches, or xenocrysts plucked from the Colorado Plateau mantle.

Green Na–Fe augitic clinopyroxene (type 2 cores) have been described from several continental alkaline basaltic provinces, particularly in monogenetic volcanic fields including the French Massif Central (Pilet et al. 2002 and references therein), the Eifel in Germany (Duda and Schmincke 1985 and references therein), the Central Italian volcanoes (Civetta et al. 1979; Barton et al. 1982), the Leucite Hills in USA (Barton and Van Bergen 1981), the Spanish central system (Orejana et al. 2007), the Isla de Trinidade (Greenwood 1998), the western Yunnan region in China (Xu et al. 2003), and many others. It is unlikely that type 2 green cores are primary mantle clinopyroxene, because they have both low Mg# and a high abundance of incompatible elements; they might, however, have formed in mantle that was metasomatized (Pilet et al. 2002). Rock (1991) interpreted such components as semi-cognate, differentiated, mantle inclusions, crystallized from an evolved lamprophyre melt and subsequently plucked and entrained into batches of more-primitive magma. Such green cores were recorded from rocks as differentiated as alkaline monzogranite of the Dariv intrusive complex in Mongolia (Bucholz et al. 2014).

Clinopyroxene megacrysts (type 1 cores) are also known from several monogenetic centres across the Colorado Plateau (Williams 1936; Lefebvre 2013; Schmidt et al. 2016), as well as in other monogenetic volcanoes worldwide (Liotard et al. 1988; Shaw and Eyzaguirre 2000; Dobosi et al. 2003). Rock (1991) considered these components as largely cognate (high-P) inclusions, crystallized from the host melt at greater depths and no longer in equilibrium with the host melt crystallized into groundmass. Under this interpretation, it is, however, difficult to explain the diffuse sieve textures, or other resorption features that pervaded the type 1 clinopyroxenes at Jagged Rocks. If we hypothesize that type 1 cores

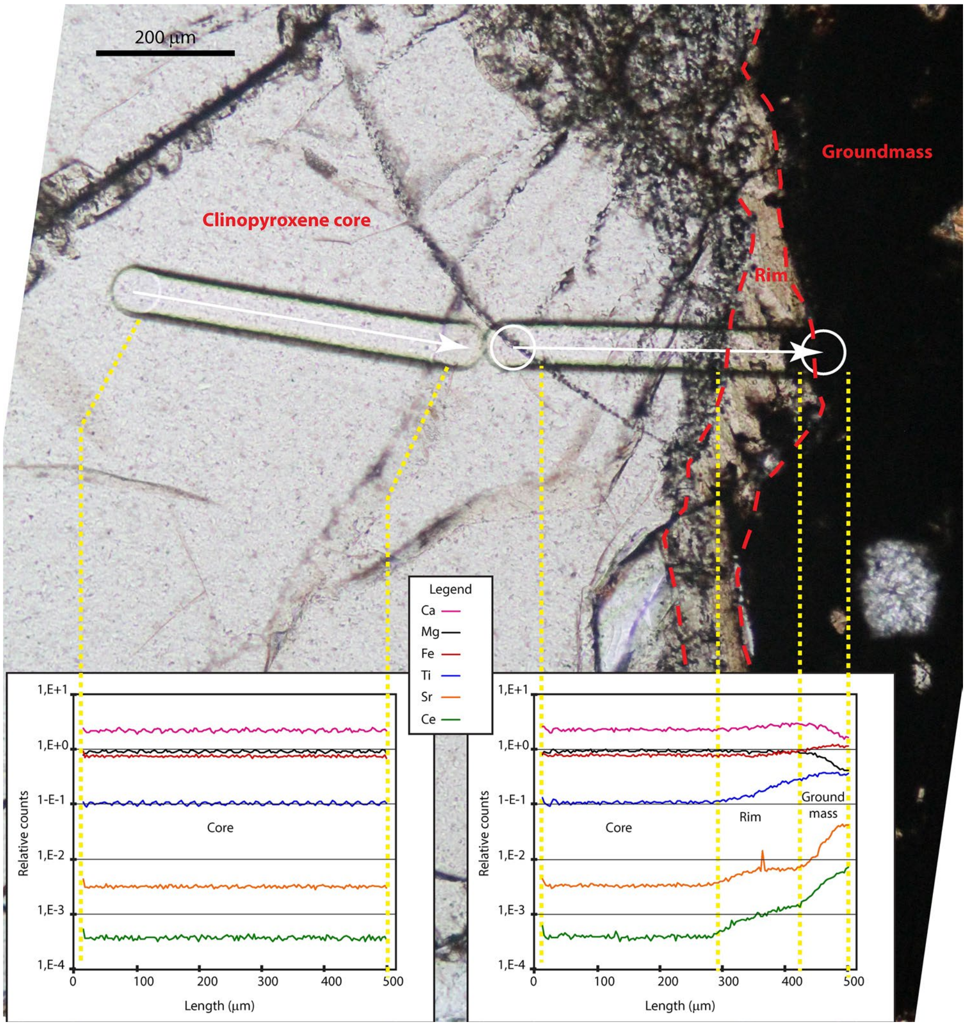

Fig. 11 Laser-ablation track across a clinopyroxene megacryst (type 1). The lines display a consistent concentration across the core, with most variation confined to the thin rim. The end of the track continued off the crystal edge into the groundmass so as to be certain of analysing the outermost part of the crystal

were resorbed after entrainment into a magma with a more-evolved composition (albeit from the same original source magma), it is uncertain why the crystal rims crystallized along a single continuous compositional trend, but major- and trace- element geochemistry supports a parental relation of type 1 clinopyroxenes (and also the phlogopite) with the host melt (groundmass), and this could result of one of the following processes. (1) Type 1 cores were crystallized from the host melt; in this case, the large size of these crystal's cores (up to few cm) and their very homogeneous compositions must require a very stable crystallization environment; for example, a large liquid-dominated reservoir with a high melt/crystal ratio to keep stable the composition of the system. This seems unlikely for a monogenetic volcano. (2) Type 1 cores are residua of the lithospheric mantle after the partial melting beneath the Jagged Rocks Complex. In this context, the sieved texture would be textural evidence that melt was extracted from the mantle source. The pressure of equilibrium calculated with the thermobarometer indicates a depth of partial melting (~ 50 km; 16 kbar) that matches that of the Moho discontinuity below this part of the Colorado Plateau as observed geophysically (Levander et al. 2011; Reid et al. 2012). These data also agree with evidence from experimental petrology revealing that phlogopite and clinopyroxene are close to liquidus at ~ 16 kbar with ~ 4.5 wt% of H_2O at the Iron–Wustite buffer (Esperança and Halloway 1987). It is also well documented that partial melting of a pyroxenite source would produce alkaline magmas (Hirschmann et al. 2003; Kogiso et al. 2004; Pilet et al. 2008).

Type 3 and type 4 clinopyroxenes, with rims overgrown on the above-mentioned type 1 and 2 cores, are the fully cognate (low-P) phenocrysts (Rock 1991). They crystallized from the host lamprophyre magma at shallow depths (~ 30 km; 8 kbar), and are in equilibrium with the enclosing groundmass. Type 3 clinopyroxenes are found mostly in intrusions of the Southern system, associated with small euhedral crystals of olivine. Their oscillatory zonation, with bands of more- and less-primitive compositions across the crystal's stratigraphy, suggests rejuvenation of the magmatic body by periodic injections of more-primitive melt. The

Fig. 12 Rare-earth and trace element spider plots illustrate the composition of the hypothetical calculated melts in equilibrium with each clinopyroxene and the phlogopite compositions. The thick blue line is the average of the groundmass composition. Partition coefficients used for the REE, Sr, Rb, Ba, Th, Nb, Zr, and Y are from Foley et al. (1996), for Li, Be, K, Pb, Hf, Ga, Ti, V, Sc, Cr, and Cu from Hart and Dunn, (1993), U from Hauri et al. (1994), Ta from Blundy et al. (1998), and Co, Ni, and Mn from Laubier et al. (2014)

crystals' growth at low pressures agrees with experimental evidences that reveal the suppression of olivine crystallization at pressures greater than 7 kbar (Barton and Hamilton 1979). This is because olivine and phlogopite are competitors and can coexist over only a small interval of pressure, temperature and water content; at higher depths and higher fO_2, the equilibrium drifts toward phlogopite, whereas at shallower depths and lower pressures, olivine is the most stable phase (Esperança and Halloway 1987; Modreski and Boettcher 1973; Barton and Hamilton 1979). This indicates that the magma of the Southern system re-equilibrated at low pressures, whereas the magma that rose up in the Northwest system, bearing phlogopite- and clinopyroxene, preserved a high-pressure assemblage.

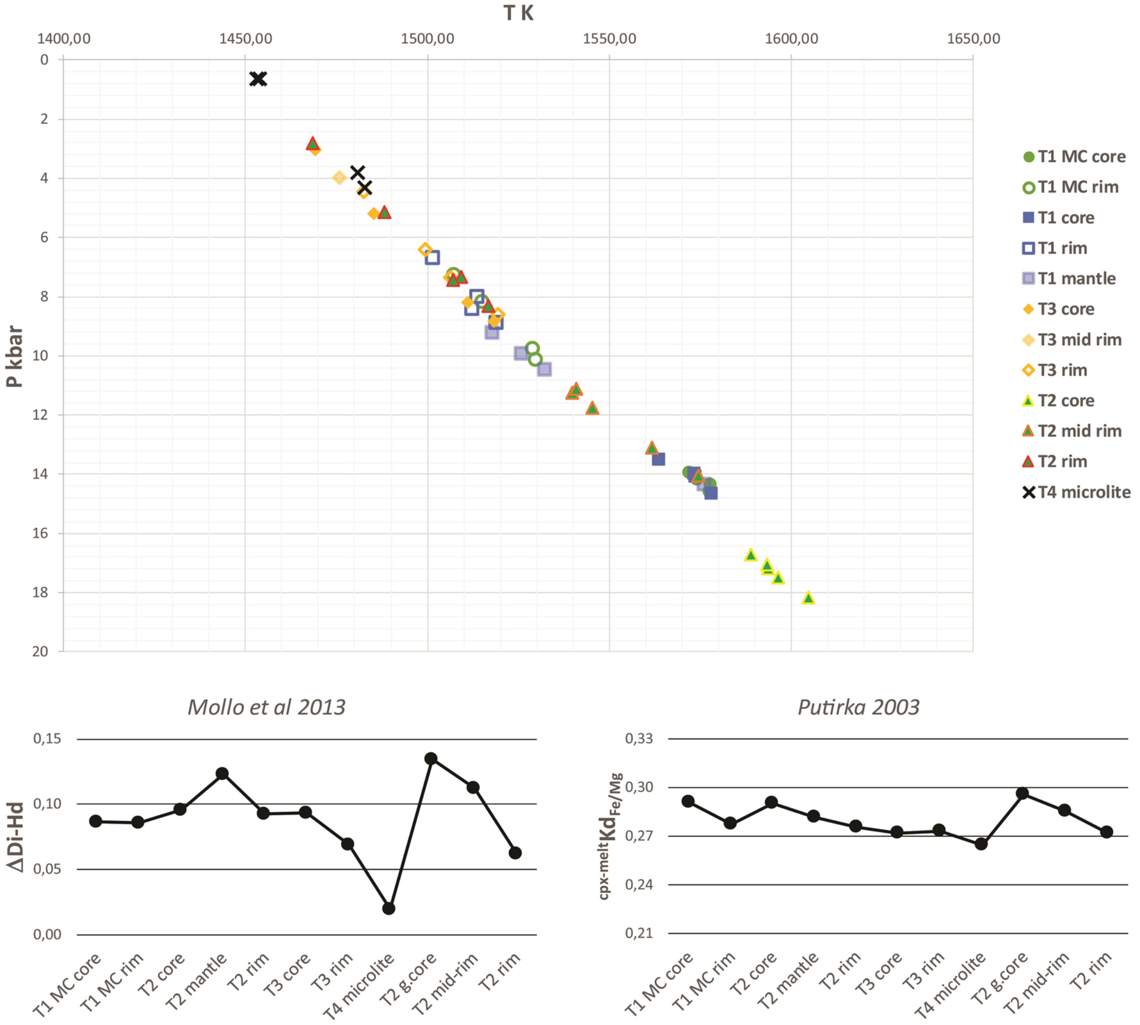

Fig. 13 Temperature (K) vs pressure (kbar) plots show the results of thermobarometry computations for the different groups of clinopyroxenes. Plots of the averages of the ${}_{\mathrm{Fe\text{–}Mg}}\mathrm{Kd}_{\mathrm{cpx\text{–}melt}}$ (Putirka et al. 2003) and the deviations among the predicted and measured diopside–hedenbergite ΔDi-Hd components (Mollo et al. 2013) are provided to investigate the equilibrium within each clinopyroxene–melt pair

Clinopyroxene rim crystallization conditions

Crystal rims overgrown on type 1 (and type 2) cores reveal a neat textural separation, as well as a distinctive geochemistry marked by depletion in Si and Mg and enrichment in Ti, Al and REE. The sharp increase in the concentration of incompatible elements is confined to the outermost portions of the crystals (~ 100 μm), which are volumetrically infinitesimal compared to the large and homogeneous type 1 cores (Fig. 11).

This trend of enrichment in incompatible elements is consistent with results from some experiments investigating the dependence of clinopyroxene compositions on magma cooling and decompression rates. These experiments (Mollo et al. 2010, 2015) reveal that increasing cooling and decompression rates cause crystals to become progressively depleted in Ca, Mg, Fe^{2+}, and Si, counterbalanced by enrichments in REE, Na, Fe^{3+}, Al, and Ti. This is because increases in Al^{3+}, and particularly Al^{iv}, cause substitutions for Si^{4+} in the tetrahedral site, and act as charge-balancing cations for the trivalent cations (REE, Zr, Th, Y, and Fe^{3+}) in the octahedral site (Francis and Minarick 2008; Scarlato et al. 2014). Increased cooling and decompression of magma induced precipitation of crystal rims in a regime largely governed by kinetic effects that modified the partitioning of elements (Mollo et al. 2011; Scarlato et al. 2014) and led to great geochemical variation. As a general model, these geochemical variations formed in response to the crystal growing next to a boundary layer of melt enriched in incompatible elements (see inset in Fig. 14) that developed at the crystal/melt interface (Lofgren et al. 2006). This layer formed where the elements rejected by the crystal accumulated within the melt just beyond the growing interface,

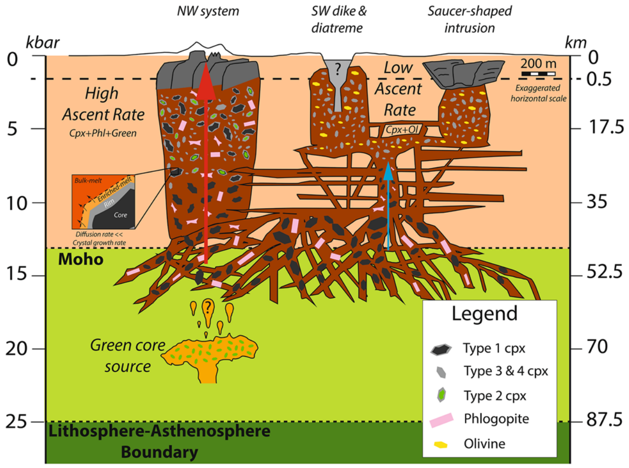

Fig. 14 Cartoon illustrating the magmatic system underpinning the Jagged Rocks Complex. Surficial features in white are eroded and inferred from Re et al. (2016). The scale of the exposed features, in grey, over the uppermost 500 m depth is exaggerated, as is the horizontal scale compared to the vertical one. The main magma body developed at about the Moho discontinuity. From that body magma was carried in dikes to feed shallow level and surface activity. Different patterns of magma ascent controlled the mineralogical assemblage, and whether crystals in the magma re-equilibrated at mid-crustal pressures (paragenesis = clinopyroxene + olivine) or were brought directly to the surface (paragenesis = clinopyroxene + phlogopite)

because diffusion through the melt was much slower than the crystal-growth rates (Coish and Taylor 1979; Gamble and Taylor 1980; Watson and Baker 1991; Watson 1994; Mollo et al. 2010 Zellmer et al. 2016).

We infer that the high ascent velocities of the magma (melt plus mixture of phenocrysts and xenocrysts) beneath the Jagged Rocks Complex generated the high decompression and cooling rates responsible for the high concentrations of incompatible elements in the clinopyroxene rims. We suggest that type 1 and 2 rims rapidly overgrew their cores during the rise of magma toward the surface. For a certain time, the crystal-grow rates must have been higher than the diffusion rates of incompatible element away from crystal/melt boundary, leading to the development of an incompatible element-rich melt interface (Lofgren et al. 2006; Mollo et al. 2015).

If the velocity of diffusion (W_c) and the size of the melt interface (x) were known, it would be possible to estimate the time of diffusion (t) for incompatible elements across the interfacial melt using the following equation:

$$t = \frac{x^2}{W_c^{\mathrm{REE}}}.$$

We calculate the time of diffusion (t) making the following assumptions. (1) The diffusion coefficient for REE (W_c) is chosen from those for basaltic melt (Zhang et al. 2010). (2) The size of the enriched-melt interface (x) can be assumed to be double the thickness of the crystal rims (r), which is about 100 µm, since the level of enrichment in the crystal rims' geochemistry is consistent with what would be expected from about 50% fractional crystallization. Based on these assumptions, the time calculated is about 11 h ("Appendix 1").

In this model, the crystal-growth rate (xl_{gr}) should be higher than the diffusion rate, so the time of diffusion can be considered of the same order of magnitude as the crystal-growth rate (xl_{gr}). Considering a 100 µm-wide crystal rim (r) and a time of growth the same as the time of diffusion (t), the crystal-growth rate is estimated as follows:

$$xl_{\mathrm{gr}} = \frac{r}{t}.$$

The calculated crystal-growth rate is 2.5×10^{-9} m/s ("Appendix 1"). For comparison, clinopyroxene growth rates in Mt Etna magmas are of the order of 10^{-10} m/s at low degrees of undercooling (< 10 °C; Armienti et al. 2013).

Finally, assuming that the growth of the crystal rims took place entirely during upward migration of magma from a source 50 km below the Jagged Rocks Complex, the average magma ascent rate was ~ 1.25 m/s ("Appendix 1"). For comparison, estimated ascent rates during the 1980 activity of Mt St Helens, from the storage zone (8–11 km) to the surface, are between 0.004 and 0.015 m/s during the lava dome phase and 2–3 m/s during the plinian phase (Rutherford and Gardner 2000). It is plausible that ascent rates at Jagged Rocks were lower at the beginning and then increased drastically, with first CO_2 at depth, and then H_2O at shallower levels, exsolving into bubbles that would have reduced magma density.

These calculations are founded on assumptions and subject to uncertainties, which include (1) the size of the enriched-melt interface, which is not fixed but migrates away from the border of the crystal during the crystallization, (2) the depth of the source, which is inferred from geothermobarometric computations, and (3) the choice of the REE diffusion coefficients, which are dependent from T, P, and composition of magma.

Differences within the plumbing system of a monogenetic volcanic complex

At the Jagged Rocks Complex, the Northwest and Southern sectors show different parageneses and different clinopyroxene textures, which reflect different conditions of crystallization related to different regimes of magma ascent.

The abundance of resorbed clinopyroxene cores (types 1 and 2) within the dike and feeder conduits of the Northwest system suggests rapid ascent of a batch of magma that dragged up high-pressure mineral phases from the source region, probably close to the Moho boundary (~ 50 km; Levander et al. 2011; Reid et al. 2012). The sieve textures of the clinopyroxene cores were generated before growth of the rims. This indicates that clinopyroxene cores are either residual xenocrysts from the mantle entrained during partial melting, or igneous crystals that began ascent in disequilibrium with their host magma, implying an antecrystic origin. Later, during a rapid ascent, the euhedral rims overgrew these cores in a kinetically driven crystallization regime with high cooling and decompression rates that led to enrichment in incompatible elements. Preservation of phlogopite megacrysts is consistent with a rapid ascent of magma through the crust that precluded their re-equilibration with melt at lower pressures and temperatures.

In contrast, the coexistence of a low-pressure paragenetic assemblage within intrusive sheets of the Southern system, which includes oscillatory-zoned clinopyroxenes (type 3) and olivine microphenocrysts, suggests re-equilibration of crystals with magma at a shallow crustal level. Both mineral phases are euhedral with crystals that do not exceed a few mm in size, and no clinopyroxene or phlogopite megacrysts are preserved. This batch of magma probably rose slowly, in stages, and stalled at shallow depths within dikes and small sills or saucer-shaped intrusions. The transformation of a dike into a sill, initiating development of a saucer-shaped structure, may occur due to changes in magma buoyancy (Francis 1982), changes in the local stress regime (Valentine and Krogh 2006; Re et al. 2015), or ascent through layers with contrasting rigidity (Burchardt 2008; Thomson and Schofield 2008; Galland et al. 2009; Magee et al. 2013; Kavanagh et al. 2006, 2015). In magma feeding, the Southern system type 1 and 2 clinopyroxene cores and phlogopite were completely dissolved or the minimum rate of magma ascent was less than the settling velocity of coarse (no more than ~ 5 cm) crystals. Low ascent rates would enhance the possibility of magma being trapped within the crust, with episodes of nil upward transport (storage) potentially providing time for either, or both, crystal dissolution and settling. Magma ascending in a slowly propagating dike has reduced ability to penetrate weak layers that are prone to viscous deformation (Schofield et al. 2012) when vertical crack propagation ceases magma may intrude laterally along bedding horizons (Muirhead et al. 2016).

The model proposed for the plumbing system below the Jagged Rocks Complex is illustrated in Fig. 14. From a source region located near the Moho at intermediate depth (~ 50 km), magma batches rose toward the surface as repeated injections. Some pulses ascended in dikes propagating at high speed, carrying both green- and megacrystic clinopyroxene cores into Jagged Rocks' Northwest system. In contrast, other magma batches rose at overall moderate-to-low rates, with stalling at low pressures/shallow depths within the middle crust. Perhaps coincidentally, when these magmas finally reached the near-surface, they produced dikes, sills, and saucer-shaped intrusions in the upper half kilometre below the surface now exposed in the Southern systems.

Conclusion

Jagged Rocks clinopyroxenes reveal a rich history of petrogenetic processes. We infer that similar complexity commonly affects magmas feeding monogenetic volcanoes. Multiple magma batches, fractional crystallization, crystal recycling, and transfer of magmas through small storage zones that form a multi-level magmatic system can strongly influence cycles of magmatic recharge and discharge during the lifetime of a monogenetic volcanic complex or a volcanic field.

Strong petrographic differences between rocks of the Northwest and Southern systems in the Jagged Rocks Complex provide evidence for a diversified plumbing system in a single small monogenetic complex (~ 2 km^2). Specifically, at least two batches of magma erupted at different times and were physically separate, though near, to one another, with a shared source at depth.

The inferred crystallization histories reveal different patterns of magma ascent toward the surface, which can yield different expressions of volcanism at the surface. Clinopyroxene overgrowths indicate that a batch of magma rose quickly (high ascent rates) to feed eruptions directly from a considerable depth and preserving the high-P mineralogical assemblage. The estimated time to accomplish transfer of magma from 50 km depth to the surface, the time preceding onset of an eruption, is on the order of half a day, which would give short warning to hazard managers. In contrast, magma that rose slower had more opportunity to become trapped for intervals within the middle crust where the crystal population re-equilibrated at lower P conditions, and again at very shallow levels in the upper half kilometre below surface, where we find intrusive rocks not only as dikes and pyroclastic massifs (conduit deposits), but also in sills and inclined sheets.

Acknowledgements This work is supported by the University of Otago Scholarship (G.Re), MBIE through subcontract to GNS Science, NZ (J.D.L.White). We thank Pietro Armienti, Marco Brenna and Michael Ort for their reviews and stimulating discussion during different stages of manuscript preparation. We further thank Bruce Kjarsgaard for the XRF geochemistry. Lastly, we gratefully acknowledge the editor Mark Ghiorso and an anonymous reviewer, whose insightful comments helped us significantly improve the manuscript.

Appendix 1: Diffusion model calculation

In this section, we would expand the three equation described in the paragraph "Clinopyroxene rim crystallization conditions"

1. To calculate the time of diffusion for incompatible elements in the interfacial melt (t), we used the equation:

$$t = \frac{x^2}{W_c^{\mathrm{REE}}},$$

x is the size of the interfacial melt layer in meters ($x = 200 \times 10^{-6}$ m), and W_c^{REE} is the diffusion coefficient for REE within a basaltic melt from Zhang et al. (2010), which is 10^{-12} m^2/s. Therefore, we obtain:

$$t = \frac{\left(200 \times 10^{-6}\,\mathrm{m}\right)^2}{10^{-12}\,\mathrm{m}^2/\mathrm{s}} = 4 \times 10^4\mathrm{s} = \sim 11\,\mathrm{h}.$$

2. To calculate the crystal-growth rate for clinopyroxene (xl_{gr}), we used the equation:

$$xl_{\mathrm{gr}} = \frac{r}{t},$$

r is the size of the rim in meters, 100×10^{-6} m, and t is the time of diffusion in seconds. Therefore, we obtain:

$$xl_{\mathrm{gr}} = \frac{100 \times 10^{-6}\,\mathrm{m}}{4 \times 10^4\,\mathrm{s}} = 2.5 \times 10^{-9}\,\mathrm{m/s}.$$

3. To calculate the average ascent velocity (v), we used the equation:

$$v = \frac{h}{t},$$

h is the depth of the source in meters, 50,000 m, and t is the time of diffusion in seconds. Therefore, we obtain:

$$v = \frac{50,000\,\mathrm{m}}{4 \times 10^4\,\mathrm{s}} = 1.25\,\mathrm{m/s}.$$

References

Alibert C, Michard A, Albarède F (1986) Isotope and trace element geochemistry of Colorado Plateau volcanics. Geochim Cosmochim Acta 50:2735–2750

Armienti P, Perrinelli C, Putirka KD (2013) A new model to estimate deep-level magma ascent rates, with applications to Mt. Etna (Sicily, Italy). J Petrol 54(4):795–813. doi:10.1093/petrology/egs085

Barton M, Hamilton DL (1979) The melting relationships of a madupite from the Leucite Hills, Wyoming, to 30 kb. Contrib Mineral Petrol 69:133–142

Barton M, Van Bergen MJ (1981) Green clinopyroxenes and associated phases in a potassium rich lava from the Leucite Hills, Wyoming. Contrib Mineral Petrol 77:101–114

Barton M, Varekamp JC, Van Bergen MJ (1982) Complex zoning of clinopyroxenes in the lavas of Vulsini, Latium, Italy; evidence for magma mixing. J Volcanol Geotherm Res 14:361–388

Billingsley GH, Block D, Redsteer MH (2013) Geologic map of the Winslow 30′ × 60′ quadrangle, Coconino and Navajo counties, Northern Arizona. USGS Scientific Investigations, Map 3247, pamphlet 25 pp, http://pubs.usgs.gov/sim/3247/

Blondes MS, Reiners PW, Ducea MN, Singer BS, Chesley J (2008) Temporal-compositional trends over short and long time-scales in basalts of the Big Pine Volcanic Field, California. Earth Planet Sci Lett 269(1–2):140–154

Blundy JD, Robinson JAC, Wood BJ (1998) Heavy REE are compatible in clinopyroxene on the spinel lherzolite solidus. Earth Planet Sci Lett 160:493–504

Boyce J, Nicholls I, Keays R, Hayman P (2015) Variation in parental magmas of Mt Rouse, a complex polymagmatic monogenetic volcano in the basaltic intraplate Newer Volcanics Province, southeast Australia. Contrib Mineral Petrol 169(2):1–21

Brenna M, Cronin SJ, Smith IEM, Sohn YK, Németh K (2010) Mechanisms driving polymagmatic activity at a monogenetic volcano, Udo, Jeju Island, South Korea. Contrib Mineral Petrol 160:931–950

Brenna M, Cronin SJ, Németh K, Smith IEM, Sohn YK (2011) the influence of magma plumbing complexity on monogenetic eruptions, Jeju Island, Korea. Terra Nova 23:70–75. doi:10.1111/j.1365-3121.2010.00985.x

Bucholz CE, Jagoutz O, Schmidt MW, Sambuu O (2014) Phlogopite- and clinopyroxene-dominated fractional crystallization of an alkaline primitive melt: petrology and mineral chemistry of the Dariv Igneous Complex, Western Mongolia. Contrib Mineral Petrol 167(4):1–28

Burchardt S (2008) New insights into the mechanics of sill emplacement provided by field observations of the Njardvik Sill, Northeast Iceland. J Volcanol Geotherm Res 173(3–4):280–288

Civetta L, Innocenti F, Lirer L, Manetti P, Munno R, Peccerillo A, Poli G, Serri G (1979) Potassic and highly potassic series of Ernic Mountains, southern Latium; petrologic and geochemical consideration. Rend Soc Ital Mineral Petrol 35:227–249

Coish RA, Taylor LA (1979) The effect of cooling rate on texture and pyroxene chemistry in DSDP Leg 34 basalt: a microprobe study. Earth Planet Sci Lett 42:389–398

Connor CB, Conway FM (2000) Basaltic Volcanic Fields. In: Sigurdsson H (ed) Encyclopedia of volcanoes. Academic Press, San Diego, pp 331–343

Dallegge TA, Ort MH, McIntosh WC (2003) Mio-Pliocene chronostratigraphy, basin morphology and paleodrainage relations derived from the Bidahochi Formation, Hopi and Navajo Nations, Northeastern Arizona. Rocky Mt Geol 40(3):55–82

Dobosi G, Downes H, Embey-Isztin A, Jenner GA (2003) Origin of megacrysts and pyroxenite xenoliths from the Pliocene alkali basalts of the Pannonian Basin (Hungary). Neues Jahrbuch für Mineralogie Abhandlungen J Mineral Geochem 178(3):217–237

Doubik P, Hill BE (1999) Magmatic and hydromagmatic conduit development during the 1975 Tolbachik Eruption, Kamchatka, with implications for hazards assessment at Yucca Mountain, NV. J Volcanol Geotherm Res 91:43–64

Duda A, Schmincke (1985) Polybaric differentiation of alkali basaltic magmas: evidence from green-core clinopyroxenes (Eifel, FRG). Contrib Mineral Petrol 91:340–353

Erlund EJ, Cashman KV, Wallace PJ, Pioli L, Rosi M, Johnson E, Granados HD (2009) Compositional evolution of magma from Parìcutin Volcano, Mexico: the tephra record. J Volcanol Geotherm Res 197(1–4):167–187

Esperança S, Halloway JR (1987) On the origin of some mica-lamprophyres: experimental evidence from a mafic minette. Contrib Mineral Petrol 95:207–216

Foley SF, Jackson SE, Fryer BJ, Greenouch JD, Jenner GA (1996) Trace element partition coefficients for clinopyroxene and phlogopite in an alkaline lamprophyre from Newfoundland by LAM-ICP-MS. Geochim Cosmochim Acta 60(4):629–638

Francis EH (1982) Magma and sediment-I Emplacement mechanism of late Carboniferous tholeiite sills in northern Britain. President's anniversary address 1981. J Geol Soc 139:1–20

Francis D, Minarick W (2008) Aluminum-dependent trace element partitioning in clinopyroxene. Contrib Mineral Petrol 156:439–451

Galland O, Planke S, Neumann ER, Malthe-Sorenssen A (2009) Experimental modelling of shallow magma emplacement: application to saucer-shaped intrusions. Earth Planet Sci Lett 277(3–4):373–383

Gamble RP, Taylor LA (1980) Crystal/liquid partitioning in augite: effects of cooling rate. Earth Planet Sci Lett 47:21–33

Ginibre C, Wörner G, Kronz A (2007) Crystal zoning as an archive for magma evolution. Elements 3(4):261–266

Greenwood JC (1998) Barian-titanian micas from Ilha da Trindade, South Atlantic. Mineral Mag 62(5):687–695

Hart SR, Dunn T (1993) Experimental cpx/melt partitioning of 24 trace elements. Contrib Mineral Petrol 113(1):1–8

Hauri EH, Wagner TP, Grove TL (1994) Experimental and natural partitioning of Th–U–Pb and other trace elements between garnet clinopyroxene and basaltic melts. Chem Geol 117:149–166

Hirschmann MM, Kogiso T, Baker MB, Stolper EM (2003) Alkalic magmas generated by partial melting of garnet pyroxenite. Geology 31:481–484

Hooten JA (1999) Phreatomagmatic diatremes of the western Hopi Buttes volcanic field, Navajo Nations, Arizona. MSc Thesis, Northern Arizona University

Houghton BF, Wilson CJN, Smith IEM (1999) Shallow-seated controls on styles of explosive basaltic volcanism: a case study from New Zealand. J Volcanol Geotherm Res 91(1):97–120

Jankovics MÉ, Harangi S, Németh K, Kiss B, Ntaflos T (2015) A complex magmatic system beneath the Kissomlyó monogenetic volcano (western Pannonian Basin): evidence from mineral textures, zoning and chemistry. J Volcanol Geotherm Res 301:38–55

Kavanagh JL, Menand T, Sparks RSJ (2006) An experimental investigation of sill formation and propagation in layered elastic media. Earth Planet Sci Lett 245(3–4):799–813

Kavanagh JL, Boutelier D, Cruden AR (2015) The mechanics of sill inception, propagation and growth: experimental evidence for rapid reduction in magmatic overpressure. Earth Planet Sci Lett 421:117–128

Kereszturi G, Németh K (2012) Monogenetic basaltic volcanoes: genetic classification, growth, geomorphology and degradation. In: Németh K (ed) Updates in volcanology—new advances in understanding volcanic systems. InTech, Rijeka, pp 3–89

Kogiso T, Hirschmann MM, Pertermann M (2004) High-pressure partial melting of mafic lithologies in the mantle. J Petrol 45(12):24072422. doi:10.1093/petrology/egh057

Laubier M, Grove TL, Langmuir CH (2014) Trace element mineral/melt partitioning for basaltic and basaltic andesitic melts: an experimental and laser ICP-MS study with application to the oxidation state of mantle source regions. Earth Planet Sci Lett 392:265–278. doi:10.1016/j.epsl.2014.01.053

Le Bas MJ (1989) Nephelinitic and basanitic rocks. J Petrol 30(5):1299–1312

Le Bas MJ, Le Maitre RW, Streckeisen A, Zanettin B (1986) A chemical classification of volcanic rocks based on the total alkali-silica diagram. J Petrol 27(3):745–750

Le Maitre RW, Streckeisen A, Zanettin B, Le Bas MJ, Bonin B, Bateman P, Bellieni G, Dudek A, Efremova S, Keller J, Lameyre J, Sabine PA, Schmid R, Sorensen H, Woolley AR (2002) Igneous rocks: a classification and glossary of terms: recommendations of the International Union of Geological Sciences Subcommission on the Systematics of Igneous Rocks. Cambridge University Press, Cambridge

Lefebvre NS (2013) Volcanology of maar—diatreme volcanic vent complexes, Hopi Buttes Volcanic Field, Navajo Nations, Arizona, USA. PhD Thesis, University of Otago, Dunedin, New Zealand

Levander A, Schmandt B, Miller MS, Liu K, Karlstrom KE, Crow RS, Lee C-TA, Humphreys ED (2011) Continuing Colorado plateau uplift by delamination-style convective lithospheric downwelling. Nature 472:461–465

Liotard JM, Briot D, Boivin P (1988) Petrological and geochemical relationships between pyroxene megacrysts and associated alkali-basalts from Massif Central (France). Contrib Mineral Petrol 98:81–90. doi:10.1007/BF00371912

Lofgren GE, Huss GR, Wasserburg GJ (2006) An experimental study of trace element partitioning between Ti–Al–clinopyroxene and melt: equilibrium and kinetic effects including sector zoning. Am Miner 91:1596–1606

Luhr JF (2001) Glass inclusions and melt volatile contents at Parı̀cutin Volcano, Mexico. Contrib Mineral Petrol 142:261–283

Magee C, Briggs F, Jackson CAL (2013) Lithological controls on igneous intrusion-induced ground deformation. J Geol Soc 170(6):853–856

McGee LE, Millet M-A, Smith IEM, Németh K, Lindsay JM (2012) The inception and progression of melting in a monogenetic eruption: Motukorea Volcano, the Auckland Volcanic Field, New Zealand. Lithos 155:360–374

Modreski PJ, Boettcher AL (1973) Phase relationships of phlogopite in the system K_2O–MgO–CaO–$A1_2O_3$–SiO_2–H_2O to 35 kilobars: a better model for micas in the interior of the earth. Am J Sci 273:385–414

Mollo S, Del Gaudio P, Ventura G, Iezzi G, Scarlato P (2010) Dependence of clinopyroxene composition on cooling rate in basaltic magmas: implications for thermobarometry. Lithos 118:302–312

Mollo S, Lanzafame G, Masotta M, Iezzi G, Ferlito C, Scarlato P (2011) Cooling history of a dike as revealed by mineral chemistry: a case study from Mt. Etna volcano. Chem Geol 288:39–52. doi:10.1016/j.chemgeo.2011.06.016

Mollo S, Putirka K, Misiti V, Soligo M, Scarlato P (2013) A new test for equilibrium based on clinopyroxene–melt pairs: clues on the solidification temperatures of Etnean alkaline melts at post-eruptive conditions. Chem Geol 352:92–100. doi:10.1016/j.chemgeo.2013.05.026

Mollo S, Giacomoni PP, Andronico D, Scarlato P (2015) Clinopyroxene and titanomagnetite cation redistributions at Mt. Etna volcano (Sicily, Italy): footprints of the final solidification history of lava fountains and lava flows. Chem Geol 406:45–54. doi:10.1016/j.chemgeo.2015.04.017

Moorhouse BL, White JDL, Scott JM (2015) Cape Wanbrow: a stack of Surtseyan-style volcanoes built over millions of years in the Waiareka–Deborah volcanic field, New Zealand. J Volcanol Geotherm Res 298:27–46

Morimoto N, Fabries J, Ferguson AK, Ginzburg IV, Ross M, Seifert FA, Zussman J, Aoki K, Gottardi G (1988) Nomenclature of pyroxenes. Mineral Mag 52:535–550

Muirhead JD, Van Eaton AR, Re G, White JDL, Ort MH (2016) Monogenetic volcanoes fed by interconnected dikes and sills in the Hopi Buttes volcanic field, Navajo Nation, USA. Bull Volcanol 78:11

Németh K (2010) Monogenetic volcanic fields: origin, sedimentary record, and relationship with polygenetic volcanism. Geol Soc Am Spec Pap 470:43–66

Nemeth K, White JDL, Reay A, Martin U (2003) Compositional variation during monogenetic volcano growth and its implications for magma supply to continental volcanic fields. J Geol Soc 160:523–530

Nemeth K, Moufti MR, El-Masry N, Qaddah A, Pécskay Z (2014) Maars over cones: repeated volcanism in the same location along fissures in western Saudi Arabian volcanic fields. In: Carrasco-Núñez G, Aranda-Gómez JJ, Ort MH, Silva-Corona JJ (eds) 5th International Maar Conference. Universidad Nacional Autónoma de México, Centro de Geociencias, Juriquilla, Querétaro, México, pp 2–3

Orejana D, Villaseca C, Paterson BA (2007) Geochemistry of mafic phenocrysts from alkaline lamprophyres of the Spanish Central System: implications on crystal fractionation, magma mixing and xenoliths entrapment within deep magma chambers. Eur J Mineral 19:817–832. doi:10.1127/0935-1221/2007/0019-1763

Ort MH, Carrasco-Nunez G (2009) Lateral vent migration during phreatomagmatic and magmatic eruptions at Tecuitlapa Maar, east central Mexico. J Volcanol Geotherm Res 181(1–2):67–77

Pilet S, Hernandez J, Villemant B (2002) Evidence for high silicic melt circulation and metasomatic events in the mantle beneath alkaline provinces: the Na–Fe-augitic green-core pyroxenes in the Tertiary alkali basalts of the Cantal massif (French Massif Central). Mineral Petrol 76:39. doi:10.1007/s007100200031

Pilet S, Baker MB, Stopler EM (2008) Metasomatized lithosphere and the origin of alkaline lavas. Science 320:916–919

Putirka K, Ryerson FJ, Mikaelian H (2003) New igneous thermobarometers for mafic and evolved lava compositions, based on clinopyroxene + liquid equilibria. Am Minerol 88:1542–1554

Re G, White JDL, Ort MH (2015) Dikes, sills, and stress-regime evolution during emplacement of the Jagged Rocks Complex, Hopi Buttes Volcanic Field, Navajo Nation, USA. J Volcanol Geotherm Res 295:65–79. doi:10.1016/j.jvolgeores.2015.01.009

Re G, White JDL, Muirhead JD, Ort MH (2016) Subterranean fragmentation of magma during conduit initiation and evolution in the shallow plumbing system of the small-volume Jagged Rocks volcanoes (Hopi Buttes Volcanic Field, Arizona, USA). Bull Volcanol 78:55. doi:10.1007/s00445-016-1050-3

Reid MR, Bouchet RA, Blichert-Toft J, Levander A, Liu K, Miller MS, Ramos CS (2012) Melting under the Colorado Plateau, USA. Geology 40(5):387–390

Rock NMS (1991) Lamprophyres. Blackie, Glasgow, p 285

Rutherford MJ, Gardner JE (2000) Rates of magma ascent. In: Sigurdsson H (ed) Encyclopedia of volcanoes. Academic Press, San Diego, pp 207–217

Scarlato P, Mollo S, Blundy JD, Iezzi G, Tiepolo M (2014) The role of natural solidification paths on REE partitioning between clinopyroxene and melt. Bull Volcanol 76:810

Schmidt ME, Schrader CM, Crumpler LS, Rowe MC, Wolff JA, Boroughs SP (2016) Megacrystic pyroxene basalts sample deep crustal gabbroic cumulates beneath the Mount Taylor volcanic field, New Mexico. J Volcanol Geotherm Res 316:1–11. doi:10.1016/j.jvolgeores.2016.02.020

Schofield NJ, Brown DJ, Magee C, Stevenson CT (2012) Sill morphology and comparison of brittle and non-brittle emplacement mechanisms. J Geol Soc 169(2):127–141

Shaw CSJ, Eyzaguirre J (2000) Origin of megacrysts in the mafic alkaline lavas of the West Eifel volcanic field, Germany. Lithos 50(1–3):75–95. doi:10.1016/S0024-4937(99)00048-1

Smith IEM, Blake S, Wilson CJN, Houghton BF (2008) Deep-seated fractionation during the rise of a small-volume basalt magma batch: Crater Hill, Auckland, New Zealand. Contrib Mineral Petrol 155(4):511–527

Sohn YK, Cronin SJ, Brenna M, Smith IEM, Németh K, White JDL, Murtagh RM, Jeon YM, Kwon CW (2012) Ilchulbong tuff cone, Jeju Island, Korea, revisited: a compound monogenetic volcano involving multiple magma pulses, shifting vents, and discrete eruptive phases. Geol Soc Am Bull 124(3–4):259–274

Streck MJ (2008) Mineral textures and zoning as evidence for open system processes. Rev Mineral Geochem 69(1):595–622

Streckeisen A (1978) Classification and nomenclature of volcanic rocks, lamprophyres, carbonatites and melilitic rocks: recommendations and suggestions, IUGS Subcommission on the systematics of igneous rocks. Neues Jahrb Mineral Abh 134:1–14

Strong M, Wolff J (2003) Compositional variations within scoria cones. Geology 31(2):143–146

Suda CE, Brookins DG, Della Valle RS (1982) Uranium and other trace element geochemistry of the Hopi Buttes volcanic province, northeastern Arizona. Econ Geol 77:l210–l1220

Thomson K, Schofield N (2008) Lithological and structural controls on the emplacement and morphology of sills in sedimentary basins. In: Thomson K, Petford N (eds) Structure and emplacement of highlevel magmatic systems. Geological Society [London] Special Publications 302, pp 31–44

Valentine GA, Cortés JA (2013) Time and space variations in magmatic and phreatomagmatic eruptive processes at Easy Chair (Lunar Crater Volcanic Field, Nevada, USA). Bull Volcanol. doi:10.1007/s00445-013-0752-z

Valentine GA, Gregg TKP (2008) Continental basaltic volcanoes—processes and problems. J Volcanol Geotherm Res 177:857–873

Valentine GA, Krogh KEC (2006) Emplacement of shallow dikes and sills beneath a small basaltic volcanic center—the role of pre-existing structure (Paiute Ridge, southern Nevada, USA). Earth Planet Sci Lett 246:217–230

Vazquez JA (1998) Maar volcanism in the Wood Chop Mesa area, Hopi Buttes Volcanic field, Navajo Nation, Arizona. MSc Thesis, Northern Arizona University

Watson EB (1994) Diffusion in volatile-bearing magmas. In: Carroll MR, Holloway JR (eds) Volatiles in magmas: reviews in mineralogy, vol 30, pp 371–411

Watson EB, Baker DR (1991) Chemical diffusion in magmas: an overview of experimental results and geochemical applications. In: Perchuk LL, Kushiro I (eds) Physical chemistry of magmas. Advances in physical chemistry, vol 9. Springer, New York, NY, pp 120–151

Wenrich KJ, Mascarenas JF (1982) Diatremes of the Hopi Buttes, Arizona: chemical and statistical analyses. US Geol. Surv. Open-File Rept. 82-0740, p 131

White JDL (1990) Depositional architecture of a maar-pitted playa: sedimentation in the Hopi Buttes volcanic field, northeastern Arizona, USA. Sediment Geol 67:55–84

White JDL (1991) Maar–diatreme phreatomagmatism at Hopi Buttes, Navajo Nation (Arizona), USA. Bull Volcanol 53:239–258

Williams H (1936) Pliocene volcanoes of the Navajo-Hopi country. Bull Geol Soc Am 47:111–172

Wimmenauer W (1973) Lamprophyre, Semilamprophyre und anchibasaltische Ganggesteine. Fortschr Mineral 51:3–67

Woolley AR, Bergman SC, Edgar AD, Le Bas MJ, Mitchell RH, Rock NMS, Scott-Smith BH (1996) Classification of lamprophyres, lamproites, kimberlites, and the kalsilitic, melilitic and leucitic rocks. Can Mineral 34:175–186

Xu Y, Huang X, Menzies MA, Wang R (2003) Highly magnesian olivines and green-core clinopyroxenes in ultrapotassic lavas from western Yunnan, China: evidence for a complex hybrid origin. Eur J Mineral 15(6):965–975. doi:10.1127/0935-1221/2003/0015-0965

Zellmer GF, Sakamoto N, Hwang S-L, Matsuda N, Iizuka Y, Moebis A, Yurimoto H (2016) Inferring the effects of compositional boundary layers on crystal nucleation, growth textures, and mineral chemistry in natural volcanic tephras through submicron-resolution imaging. Front Earth Sci 4(88):1–7. doi:10.3389/feart.2016.00088

Zhang Y, Ni H, Chen Y (2010) Diffusion data in silicate melts. Rev Mineral Geochem 72:211–408